Precipitate evolution and strengthening mechanisms in L-PBF GRCop-42 under thermal aging

Materials & Design 264 (2026) 115722

Contents lists available at ScienceDirect

Materials & Design

journal homepage: www.elsevier.com/locate/matdes

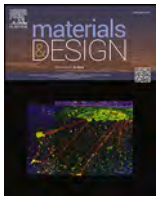

Precipitate evolution and strengthening mechanisms in L-PBF GRCop-42 under thermal aging

Stefano Felicioni [a,b,*], Adrian Barbosa Cantu [c], Elisa Padovano [a,b], Angela Veiga [c], Miren Aristizabal [c], Nerea Ordás [c], Federica Bondioli [a,b]

[a] Department of Applied Science and Technology, Politecnico di Torino, Corso Duca degli Abruzzi 24, 10129 Torino, Italy
[b] Consorzio Interuniversitario Nazionale per la Scienza e Tecnologia dei Materiali (INSTM), Via G. Giusti 9, 50121 Firenze, Italy
[c] Ceit-BRTA and Tecnun (Universidad de Navarra), Paseo de Manuel Lardizábal 15, 20018 Donostia-San Sebastián, Spain

ARTICLE INFO

Keywords:
Additive Manufacturing
Laser Powder Bed Fusion
GRCop
Precipitation behaviour
DAHT
CuCrNb
Phase Transformation
Microstructure
Mechanical properties

ABSTRACT

High-performance copper alloys are increasingly sought across multiple industries, including medical, power and energy, advanced tooling, and manufacturing, due to their exceptional thermal conductivity, oxidation resistance, and mechanical strength. Among these, GRCop-42 (CuCrNb) has gained strategic importance especially in aerospace engineering, where materials must endure extreme thermal gradients and mechanical loads in high-heat-flux environments, most notably in reusable rocket propulsion and combustion chamber applications. The performance of GRCop-42 is largely controlled by a fine dispersion of Cr_2Nb Laves phase particles, which strengthen the alloy through precipitation and dispersion-hardening mechanisms.

Additive manufacturing techniques, especially Laser Powder Bed Fusion (L-PBF), offer the potential to further refine the microstructure due to their inherently rapid solidification rates. This study investigates the microstructural evolution of L-PBF processed GRCop-42, with a particular focus on the thermal stability and coarsening behaviour of Cr_2Nb precipitates under various aging conditions. By employing advanced microscopy techniques (FESEM and TEM) alongside crystallographic analyses (XRD and EBSD), this research aims to elucidate the mechanisms of Ostwald ripening and their influence on the alloy strengthening behaviour.

1. Introduction

The aerospace industry faces many complex challenges, among which one of the most critical is the exorbitant cost associated with space exploration. To mitigate this issue, the development of reusable launch vehicles, exemplified by the Space Shuttle program, was envisioned as a fundamental strategy for reducing overall mission expenses. Nevertheless, despite the conceptual validity of this approach, its practical implementation remains hindered by significant technological and engineering limitations. These include the need to design components capable of operating reliably under extreme conditions while ensuring sufficient durability over multiple cycles [1]. For instance, a typical rocket nozzle is subjected to extremely high-energy fluxes and intense mechanical loads, leading to considerable thermal stress and progressive material degradation. These harsh operational environments substantially reduce the service life of nozzle components, undermining the economic viability of reusability and highlighting the need for advanced materials and innovative cooling or protective strategies. When heat conduction through the material is insufficient to maintain safe thermal gradients, high-melting-point refractory alloys, such as those based on molybdenum and tungsten, may be required due to their exceptional thermal resistance. However, their high density and poor workability present significant drawbacks in aerospace applications, where mass efficiency is a primary concern [2].

According to the literature, the best trade-off between the mechanical performance and thermal tolerance has historically been found in Ni-based superalloys. However, their relatively low thermal conductivity limits their effectiveness under extreme thermal flux conditions. Consequently, research has shifted towards high-performance copper alloys. Early examples include NARloy-Z (Cu-Ag-Zr) and GlidCop-A15 (Cu-0.03% Al_2O_3) [3]. More recently, Cu-Cr based systems have emerged as leading candidates [3,4], particularly when alloyed with elements such as Nb, Zr, and Ag. Among these, the Cu-Cr-Nb ternary system has attracted particular attention for its structural reliability in high temperature environments. NASA has developed and patented specific formulations of this system under the commercial name of

* Corresponding author.
E-mail address: stefano.felicioni@polito.it (S. Felicioni).

https://doi.org/10.1016/j.matdes.2026.115722
Received 2 September 2025; Received in revised form 28 January 2026; Accepted 23 February 2026
Available online 24 February 2026

GRCop alloys, most notably GRCop-84 and GRCop-42, where the numbers refer to the combined atomic percentages of the alloying elements. These alloys are also particularly notable for their low thermal expansion, along with enhanced oxidation and corrosion resistance [5–7].

The mechanical properties of both the GRCop alloys are primarily influenced by Cr_2Nb Laves phases, which possess a Face Centered Cubic (FCC) crystal structure corresponding to the C15 Strukturbericht designation [8,9]. These intermetallic phases tend to form relatively easily during solidification or subsequent thermal treatments, primarily due to favorable thermodynamic conditions within the Cr-Nb system, namely, a negative Gibbs free energy of formation and strong chemical affinity between the constituent elements. Although the strengthening effect of the Cr_2Nb intermetallic in these alloys remains an active area of investigation, two primary mechanisms have been proposed: precipitation strengthening and dispersion strengthening [10]. Both mechanisms involve interactions with dislocations moving through the matrix. Precipitation strengthening relies on the formation of a secondary phase from a supersaturated solid solution, where coherent or semi-coherent particle interfaces hinder dislocation motion. In contrast, dispersion strengthening involves the intentional introduction of a stable secondary phase during processing, which acts as an obstacle, increasing the effective stress required for plastic deformation [11]. A review of the literature indicates that while Cr and Nb exhibit complete mutual solubility in the liquid phase, their solubility in solid copper is markedly limited [12,13]. Cr reaches a maximum solubility of approximately 0.85 at. % at the eutectic temperature (~1075°C), while Nb shows an extensive immiscibility gap. According to the Cu-Nb phase diagram, their mutual solubility becomes negligible above 1200°C across a broad compositional range. This limited solubility promotes the formation of Nb-rich dispersoids during solidification, contributing to a potential initial dispersion strengthening effect.

However, achieving enhanced strengthening while simultaneously preserving the purity of the copper matrix and its desirable thermal and electrical properties require extending the solid solubility limits of the alloying elements. This can be accomplished only through rapid solidification, which facilitates the formation of a supersaturated solid solution and enables fine Cr_2Nb precipitation during the following consolidation steps or post build heat treatments [14,15]. Given the significant hardness contrast between the matrix and the precipitates, dislocations are unable to shear the particles. As a result, the precipitation strengthening in this material is primarily governed by coherency strain and Orowan bypass mechanisms. This implies that particle size, distribution, and morphology are critical parameters in determining the alloy overall strengthening effectiveness [16].

GRCop alloys are also known for their exceptional microstructural stability, primarily attributed to the slow coarsening kinetics of the Cr_2Nb in the solid state [14]. This characteristic offer both advantages and limitations. On the one hand, the thermal stability supports the retention of mechanical properties even after prolonged exposure to high temperatures. On the other hand, if clustering occurs during processing, the resulting coarse particles are essentially insoluble, even above the melting temperature of the Cu matrix, and even high temperature heat treatments, such as at 900°C, only promote further coarsening rather than dissolution. To mitigate these effects, the conventional production route for GRCop alloys typically begins with gas atomization, followed by extrusion or hot isostatic pressing (HIP) [5,17]. Gas atomization is widely adopted in industry due to its relatively low costs, high production capacity, and rapid cooling rates of approximately 104 K/s after solidification of atomized particles, which help suppress undesirable phase clustering during solidification.

For processing-related reasons, GRCop-42 has recently emerged as the preferred choice over GRCop-84 for rocket engine combustion chamber liners, primarily due to its higher thermal conductivity. When produced via conventional methods, GRCop-42 exhibits a 5–8% improvement in both thermal conductivity and ductility compared to GRCop-84, while maintaining comparable mechanical strength [6]. Although these improvements come at the expense of reduced fatigue strength, GRCop-42 nonetheless satisfies the performance requirements for reusable components exposed to high-heat-fluxes [18].

While conventional production methods have demonstrated reliable performance over the years, they are inherently limited by the complexity of multi-stage processing. In this scenario, metal additive manufacturing (AM) technologies, such as Laser Powder Bed Fusion (L-PBF), Laser Directed Energy Deposition (L-DED), Cold Spray (CS), and Binder Jetting (BJ) [19], are currently regarded as some of the most promising alternatives. These methods enable single step fabrication and offer maximum design freedom. Moreover the localized melting characteristic of AM, particularly in L-PBF, enables extremely high cooling rates, reaching up to 10^5–10^6 K/s [20]. Such rapid solidification fosters significant metallurgical improvements, including suppression of Cr_2Nb growth and overall microstructural refinement, as demonstrated by Gruber *et al.* [21], Demeneghi et *al.* [22] and by Gradl *et al.* [18,19].

In this study, GRCop samples were fabricated using L-PBF. During the L-PBF process, thin layers of powder are evenly spread over a build plate and selectively melted by a fiber laser beam, typically operating in the near-infrared wavelength range, to form the desired geometry. After each layer is completed, a new layer of powder is spread, and the process is repeated layer by layer until the part is fully built.

This study aims to investigate the L-PBF processing implications on the microstructural evolution of the GRCop-42 alloy, with a specific focus on the thermal evolution of Cr_2Nb particles. The research focuses on the characterization of this Laves phase in terms of size and morphology, evaluating the microstructural changes as a function of temperature and aging time. A key objective is to understand the mechanisms of particle coarsening and dissolution, commonly known as Ostwald ripening, as the growth rate of dispersed particles directly impacts the long-term thermal stability of the alloy (at elevated temperatures, around 0.5 of melting temperature) and its associated overall strengthening mechanisms.

2. Materials and methods

2.1. Materials

Gas-atomized powder of GRCop-42 was produced at Ceit research center (Spain) in a PSI Hermiga 75/3 (*Phoenix* Scientific Industries Ltd., UK) VIGA close coupled gas atomizer. The composition, determined by Inductively Coupled Plasma Optical Emission Spectroscopy (ICP-OES Varian 725-ES, Agilent Technologies, CA, USA), is in compliance with the compositional ranges defined by NASA[18] (Table 1).

As depicted in Fig. 1a, the atomized powders exhibit a spherical morphology, with only a minimal presence of satellite particles and agglomerates. The powder internal microstructure is characterized by equiaxed grains (Fig. 1b) and a homogeneous distribution of rounded Cr-Nb secondary phases of submicron size throughout the entire cross-section, as assessed by EDS maps (Fig. 1d).

For L-PBF specimen fabrication, powders within a particle size range of 20–63 μm were selected by sieving. The particle size distribution (PSD), determined via dynamic image analysis using a Sympatec QICPIC/L02 system (Sympatec GmbH, Germany), follows a lognormal distribution, with a median particle size (D_{50}) of 33.25 μm (Fig. 1c). The laser processability of the powder in the near-infrared range (1070 nm) was assessed using a Cary 500S UV–Vis-NIR spectrophotometer (Agilent Technologies, CA, USA), which measured an optical absorption value of

Table 1
CEIT GRCop-42 powder chemical composition.

Composition (wt. %)		Impurities (ppm)		
Cu	**Cr**	**Nb**	**C**	**O**
Bal.	3,39	2,99	294	239

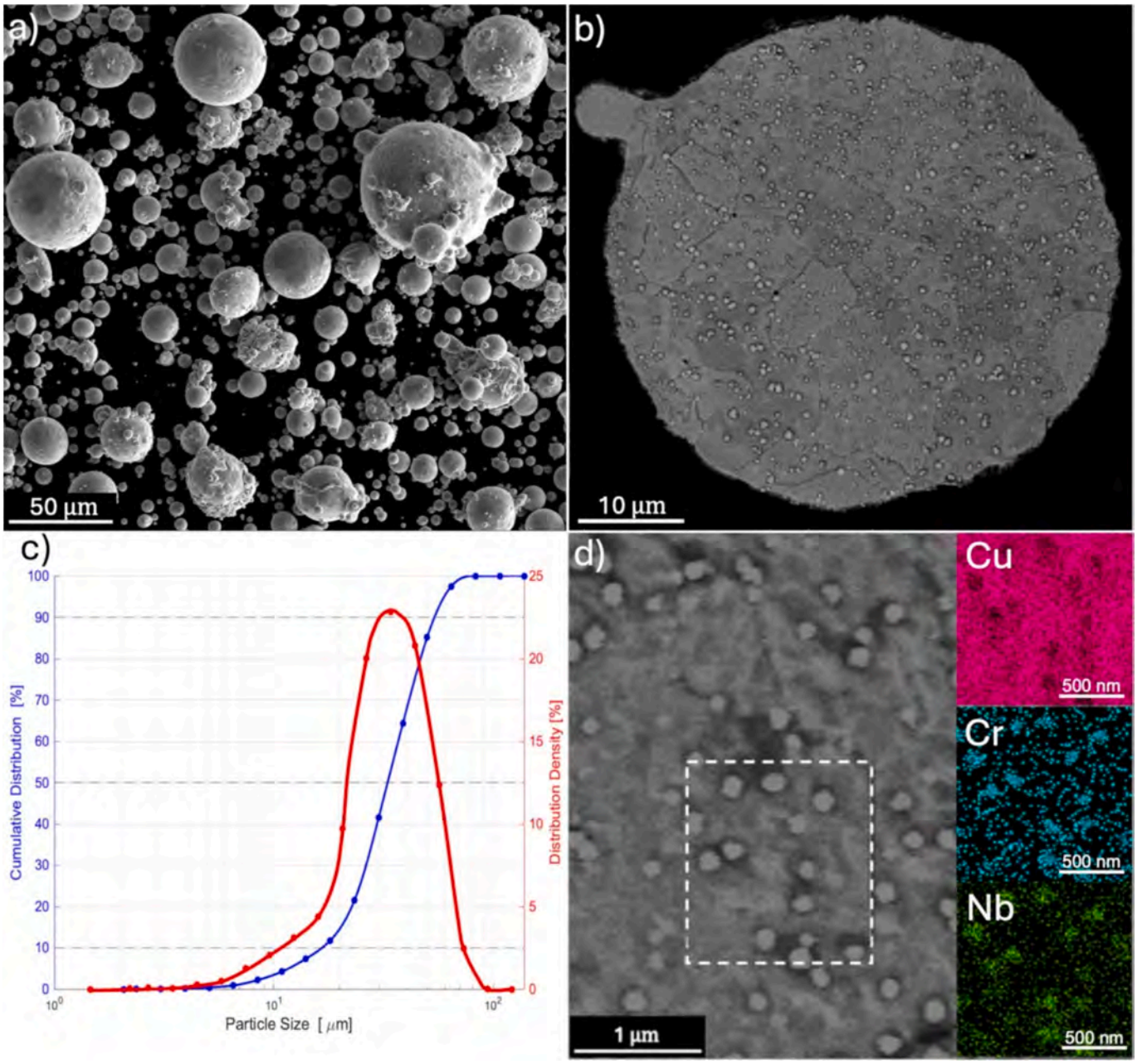

Fig. 1. A) fe-sem micrographs of the grcop-42 as atomized powder displaying the good sphericity in all the size ranges; b) representative cross section of the grcop-42 powder showing equiaxed microstructure decorated by a fine dispersion of the cr-nb secondary phase; c) psd of the processed batch after sieving; d) eds compositional mapping of the highlighted area.

43%.

2.2. Experimental

All samples were built in a Renishaw Ren AM 500-Flex L-PBF system featuring a laser spot of 80 µm and able to operate up to 500 W of laser power in the infrared range. The machine operates with a counter-rotating roller recoater and an argon inert gas atmosphere, supported by a laminar gas flow across the build plate to minimize spatter redeposition and oxidation.

Nearly fully dense samples (up to 99,7% of relative density) were fabricated with the process parameters listed in Table 2. Process optimization was performed experimentally on cubic specimens with an edge length of 10 mm using a central composite design (CCD) to

Table 2
Processing parameters utilized in this work, and relative density measured with imaging methods and Archimedes.

Power [W]	Scanning Speed [mm/s]	Hatching Distance [mm]	Layer Thickness [mm]	VED [J/mm^3]	Relative Density Imaging [%]	Relative Density Archimedes [%]
235	600	0.07	0.04	139.88	99.72	99.34

evaluate multiple parameter combinations across a volumetric energy density (VED) range of 75–250 J/mm^3.

The VED was calculated using the relation:

$$VED = \frac{P}{v \times HD \times lt},$$

where P is the laser power, v is the scanning speed, HD is the hatch distance, and l_t is the layer thickness

The preliminary densification assessment was carried out in accordance with ASTM B311–22 [23], based on Archimedes' principle. Mass measurements were performed with an analytical balance Mettler Toledo – ML304T/00 (Mettler Toledo International Inc., OH, USA), with a resolution of 0.10 mg and equipped with a dedicated density measurement setup. To validate the measurements, a statistical analysis was conducted through image-based examination of representative cross-sections. Samples were sectioned along planes both perpendicular and parallel to the build direction, following standard metallographic preparation procedures. For each sample, 30 images were collected at 50x magnification using a Leica DMI 5000 M optical microscope (Leica Microsystems GmbH, Germany) and subsequently analyzed using ImageJ software.

To investigate precipitation behavior and microstructural evolution, the optimized samples underwent direct aging heat treatments (DAHT) at temperatures of 400 and 500°C for 30, 60, 180, 300 and 480 min. The selection of the heat treatment temperature and time was guided by thermal analysis via Differential Scanning Calorimetry (DSC), performed using a NETZSCH Jupiter STA 449 FS (NETZSCH Group AG, Germany). All DSC analyses were performed under an argon atmosphere, with a heating rate of 10 K/min up to 1200°C.

Microstructural analysis of both as-built (AB) and DAHT-treated samples required chemical etching to reveal microstructural features. A solution consisting of 1.5 g $FeCl_3$, 10 ml HCl, and 30 ml distilled H_2O was applied for 10 s to reveal grain morphology. Alternatively, Kalling's reagent was applied for 2 to 5 s to enhance the visibility of melt pool structures.

Precipitation morphology and microstructural characteristics were further examined via scanning electron microscopy (SEM). A ZEISS Σigma 560 VP (Carl Zeiss AG, Germany) field emission gun, equipped with energy dispersive spectroscopy (EDS), and a TESCAN S9000G (Tescan Group a.s., Czech Republic), equipped with electron backscatter diffraction (EBSD) detectors, were utilized for this purpose. EBSD analysis facilitated the evaluation of average grain size and median misorientation angle. Data processing was carried out using Aztec Crystal software (Oxford Instruments plc., UK). Grain boundaries were defined as regions with misorientation angles greater than 15°, while sub-grain boundaries were characterized by misorientation angles below this threshold.

Additionally, Kernel Average Misorientation (KAM) analysis was performed to assess local misorientation, ranging from 0.5° to 5°, relative to adjacent pixels. This misorientation angle (θ [rad]) was subsequently used to estimate the dislocation density ($\rho 0$) according to the following equation[24]:

$$\rho_0 = \frac{2\sqrt{3}\theta}{3bs} \quad (1)$$

where b [m] is the Burgers vector (assumed to be 0.256 nm for a Cu matrix [25]) and s [m] is the step size employed in the EBSD mapping (0.2 μm).

For further microstructural characterization, a Thermo Scientific TALOS F200X transmission electron microscope (TEM) (Fisher Scientific co., Ma USA), operated at 200 keV and equipped with a double tilt specimen holder cooled with liquid nitrogen, was used. TEM thin foils were mechanically prepared by polishing down to 0.25 μm, followed by punching, dimpling on both sides, and final thinning to electron transparency using a Technoorg UniMill precision ion polishing device (Technoorg Linda Co. Ltd., Hungary) operated at 12V. The Ar^+ twin ion beam was set to progressively decrease the incident angles from 8° to 4° respect to the thin disc surface.

Statistical evaluations of the mean size, distribution, and volume fraction of the quasi-spherical Cr_2Nb particles were carried out using connected component analysis on UHR SEM images, processed with Leica Image pro-plus image analysis software.

Phase content under each condition was determined via X-Ray micro-diffraction analysis with a Buker D8 Advance micro-diffractometer (Bruker Co., MA USA) operating with Cu K α radiation. The setup was operated at 40 kV and 40 mA, with a step-size of 0.02° over a 2θ range between 30° and 100°. Phase identification and quantification were conducted using Bruker DIFFRAC.EVA and MAUD software, based on the Rietveld method.

Finally, mechanical properties of the material in all the analysed conditions were estimated through Vickers microhardness testing, performed using a QATM Qness – Q30 A + apparatus (QATM GmbH, Germany) with a 100gf load applied for 15 s, following the guidelines outlined in ASTM E384 [26].

3. Results and discussion

3.1. As-Built (AB) samples microstructure

Fig. 2 displays representative micrographs of cross-sections perpendicular to the build direction for the optimized specimens in the As-Built (AB) condition. From a macroscopic perspective, this cross-section distinctly reveals deep and interconnected molten pools, reflecting the layer-wise L-PBF build architecture (Fig. 2b), with columnar grains extending across multiple layers (Fig. 2a). The morphology of the melt pools observed in Fig. 2b is indicative of keyhole mode melting rather than conduction mode melting. Furthermore, the distribution of the residual porosity, characterized by high sphericity and mostly located at the peripheries of the scanned tracks (white arrows), further supports its formation via keyhole mechanism. This phenomenon is commonly observed during the processing of highly reflective alloys with infrared laser sources, where the available processing window is typically narrow and requires high-power input. Among the various process parameters, laser power plays a particularly significant role in determining melt pool penetration depth, which generally increases linearly with higher power levels. [27].

Under normal conditions, where melting is conduction-controlled, process efficiency is primarily influenced by the optical absorption properties and thermal conductivity of the material. In such cases, most of the reflected laser energy is lost to the surrounding environment. In highly conductive materials, such as copper-based alloys, rapid heat dissipation leads to shallow melt pools and poor bonding between successive layers. In contrast, within the keyhole regime, melting efficiency is primarily influenced by the characteristics of the keyhole itself, as the nature of laser reflection changes significantly upon its formation. Similarly to observations in laser welding, the formation of a keyhole gives rise to complex multiple reflection phenomena, which enhance energy absorption and modify heat distribution within the melt pool [28]. However, maintaining a stable keyhole regime in L-PBF processes is particularly challenging, as it requires a delicate balance between the recoil pressure induced by metal evaporation (promoting keyhole formation) and various counteracting forces, including surface tension, fluid convection, hydrostatic pressure, and gravity [29,30]. When a stable keyhole mode is achieved through process optimization, the joining efficiency can be described as "cavity-enhanced" [31]. In this regime, volume expansion at the lower section of the keyhole increases the frequency of laser beam reflections, enhancing local energy absorption and promoting continuity between layers. However, the thermophysical properties of the material under investigation facilitate rapid heat dissipation, reducing the time available for keyhole closure at

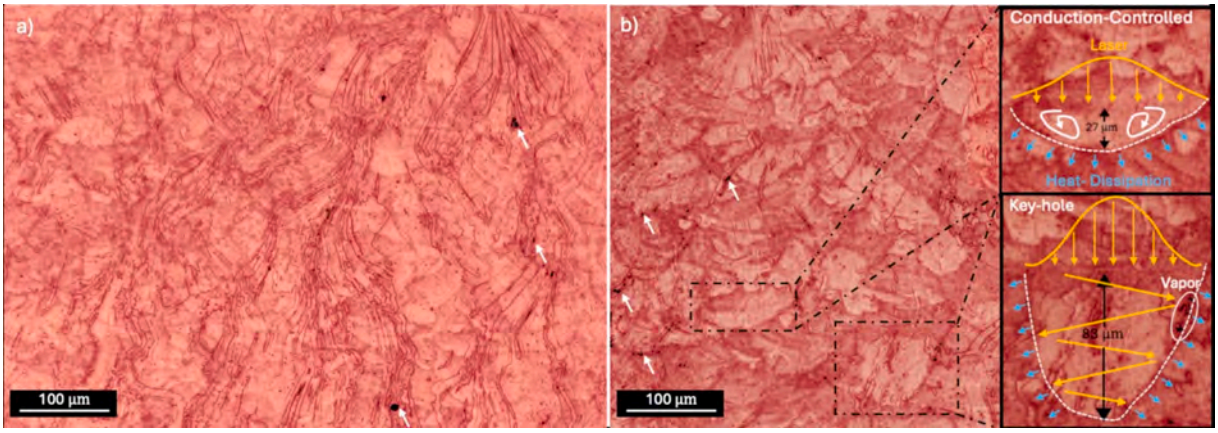

Fig. 2. Representative micrograph of the optimized samples along the direction parallel to the growth direction, displaying: a) columnar grain morphology extending across multiple layers characteristic of the L-PBF process; b)the layered structure along with meltpool borders highlighting in the insets their uneven shapes and size distribution caused by the infrared laser processing. The keyhole formation thanks to multiple reflection phenomena determines an increased meltpool penetration up to 3 times deeper than normal conduction, with minor traces of vapor induced porosity.

the melt pool and resulting in an uneven energy distribution along the keyhole walls [32]. This effect, combined with the low surface tension of the molten copper, the primary constituent of the GRCop-42 alloy, reported to be approximately two-thirds that of liquid iron [33], makes the molten metal more sensitive to laser energy at the gas/liquid interface during deep-penetration processing. As a result, the reduced time available for the liquid metal to fill gaps before solidification increases the likelihood of vapor bubble entrapment, ultimately resulting in keyhole-induced porosity.

The unstable energy dynamics within the keyhole regime have a significant impact on the resulting microstructure. In general, during solidification, the morphology and size of the microstructure mainly depend on two factors: the temperature gradient (G) and the solidification rate (R), which, as described by Geng *et al.* [34], can be expressed as:

$$G = \nabla T \bullet \hat{n} \tag{2}$$

$$R = V \bullet \hat{i} \tag{3}$$

where $\hat{n}$ is the unit normal vector perpendicular to the solid liquid interface, and $\hat{i}$ is the unit vector in the scanning direction. The interplay between these two factors determines both the morphology (expressed by the ratio G/R) and the size (given by the product G•R) of the resulting microstructure [35,36]. In general, low G/R values favor the formation of equiaxed structures, while high G/R values promote the development of columnar grain structures.

Fig. 3 presents the EBSD map of a representative molten pool, clearly highlighting volumetric expansion in its bottom region. The observed grain morphology consists of a combination of large columnar grains and smaller equiaxed grains. At the melt pool borders, where heat conduction dominates, the thermal gradient (G) reaches its maximum, while the solidification front velocity (R) is minimal during the initial stages of solidification. These conditions lead to high G/R values that promote the formation of columnar grains.

This effect becomes even more pronounced in the upper region of the melt pool, where a distinct closing tendency is observed (Fig. 3a). In contrast, within the central area of the melt pool, solidification parameters alone are insufficient to fully describe the resulting microstructure. In this zone, multiple laser reflections enhance local energy absorption, which reduces the spatial thermal gradient, increases the solidification rate, and intensifies subcooling. Additionally, the flow field becomes highly turbulent. This turbulence, combined with the high cooling rate, promotes grain fragmentation and further microstructural refinement. The resulting fine grains act as nucleation sites, as seen in Fig. 3b–c,

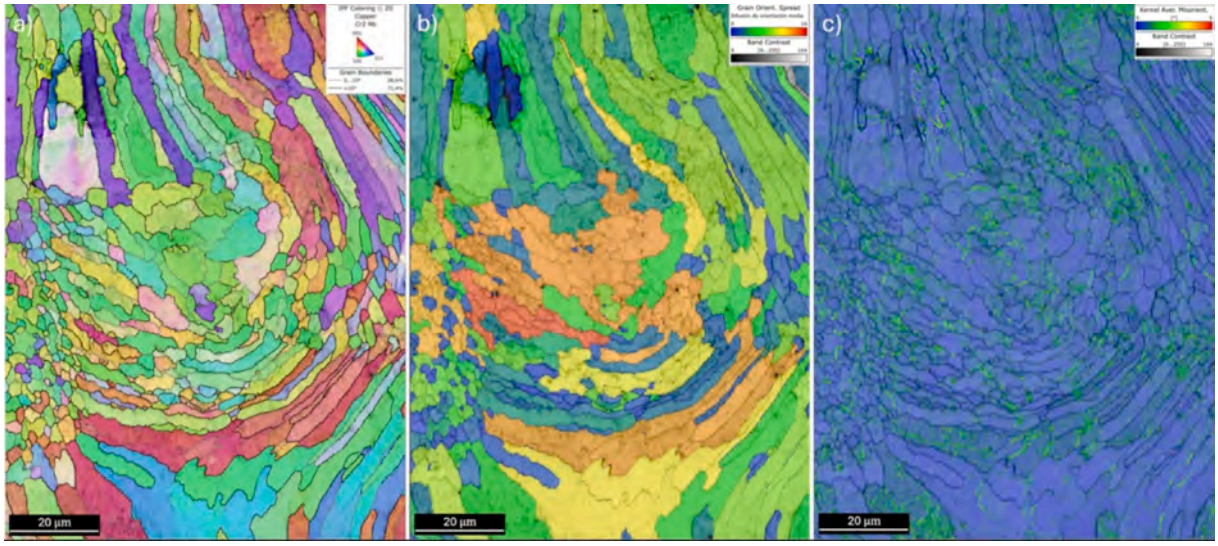

Fig. 3. Optimized sample EBSD maps of a representative molten pool: a) IPF pole figure, b) Grain Orientation Spread; c) Kernel Average Misorientation.

which display smaller structures characterized by low internal stress and minimal local misorientation.

These variations in cooling rate across different regions of the melt pool also affect precipitation behavior. In the AB condition, this results in a marked bimodal distribution of secondary phases with significant variation in both morphology and size. As shown in Fig. 4, the microstructure within the melt pool cores (referred to as A zone), which experience a more rapid cooling, exhibits a population of fine, uniformly dispersed precipitates typically ranging from 20 to 30 nm. In contrast, coarser precipitates, often exceeding 80–100 nm, are clustered along the melt pool boundaries (referred to as B zone), where cooling rate is significantly lower. These larger clusters form within the mushy zone and highlight the localized nature of precipitation, driven by thermal gradients during solidification. Note that these precipitates are finer than those observed in the atomized powder (Fig. 1d).

3.2. Precipitate identification structure and morphology in AB samples

An in-depth characterization of the secondary phases was conducted through advanced microscopy, which revealed the presence of numerous nearly spherical particles (Fig. 5a). In particular, the STEM maps shown in Fig. 6 confirm the composition of these particles as Cr_2Nb, based on the measured elemental ratios.

Regarding the crystallographic arrangement of the dispersoids, Fast Fourier Transform (FFT) analysis reveals a Face-Centred Cubic (FCC) structure exhibiting both coherent and semi-coherent interfaces with the Cu matrix. Fig. 5b and 5d show crystallographic Orientation Relationship (OR) in reciprocal space between the precipitates and the matrix, defined as: $(1\bar{1}\bar{1})Cu \| (1\bar{1}\bar{1})Cr_2Nb$ and $(0\bar{2}\bar{2})Cu \| (0\bar{2}\bar{2})Cr_2Nb$. This OR indicates a high degree of crystallographic alignment between the two phases, which differs from the classical cube-on-cube configuration. The crystallographic coherence is maintained along the [111] direction, a feature commonly observed in early-stage Guinier–Preston Zone (GPZ)-like precipitates (Fig. 5c). This is further corroborated by the presence of Moiré fringes in the Cu matrix, which are also aligned along the same crystallographic direction.

The atomic mismatch can be estimated from the HRTEM image reported in Fig. 7 by applying Eq. (4), which calculates the relative difference in atomic plane spacing:

$$\delta = \frac{|2(d_1 - d_2)|}{(d_1 + d_2)} \tag{4}$$

where d_1 and d_2 represent the interplanar spacings of the Cu matrix and the secondary Cr_2Nb strengthening phase, respectively. The measured values are $d_1 = 0.201nm$ and $d_2 = 0{,}209nm$, resulting in a mismatch (δ) of 0,039. This low degree of mismatch confirms the good crystallographic alignment between the two phases. The observed crystallographic arrangement is in good agreement with previous studies on similar alloys, which report the same solidification arrangement [37,38].

3.3. As built samples thermal evolution

DSC analysis was performed on the AB samples (Fig. 8) in order to investigate the thermal evolution of the alloy, evaluate the precipitation kinetics in the AB condition, and identify the most suitable post post-build heat-treatment parameters. The DSC curve reveals four exothermic peaks (I, II, III and IV, respectively) and a prominent endothermic peak (V). These thermal events provide two key insights: first, they support the retention of a supersaturated solid solution within the matrix, resulting from the extremely rapid cooling rates inherent to the process; second, they help elucidate the precipitation sequence during aging in the Cu-Cr-based alloy system. According to the literature, two main precipitation pathways are possible for Cu-Cr alloys [39,40]:

- Supersaturated solid solution → nanoscale Cr-rich clusters → coherent Cr GPZ → BCC Cr phase → incoherent BCC Cr phase
- Supersaturated solid solution → Cr GPZ → FCC Cr phase → ordered FCC Cr phase → BCC Cr phase

The latter sequence aligns with the phase transformations observed in the CuCrNb alloy under investigation. In this context, peak I can be attributed to the nucleation of the C15 *Cr2Nb* phase, potentially followed by the minor formation of *Cr3Cu* (peak II). In fact, Yang *et al.* [37], based on time–temperature–transformation (TTT) diagrams for similar alloys, reported that this phase begins to form at approximately 450°C. At elevated temperatures, near 500°C, diffusive phase transformations become more prominent, potentially resulting in the precipitation of the high temperature metastable C14 *Cr2Nb* hexagonal phase (peak III and

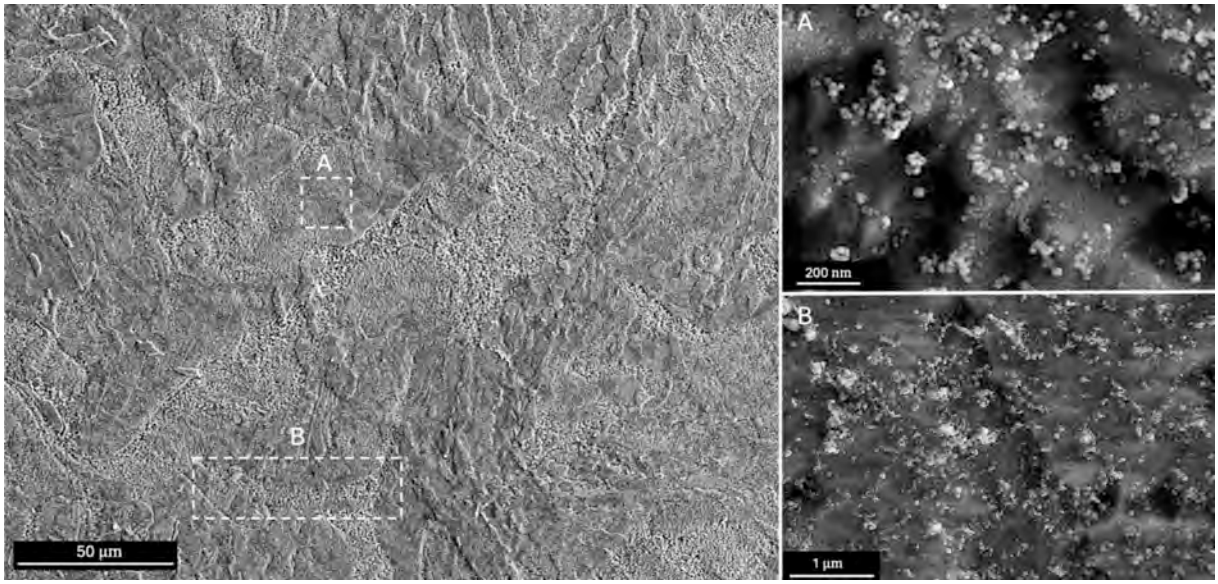

Fig. 4. FESEM micrographs of as-built samples showing the bimodal precipitation behaviour in different areas of the melt pool: Meltpool core (A zone), thanks to the higher cooling rate, displays a more homogeneous distribution of spherical nanoprecipitation; the melt pool borders (B zone), which experience a lower cooling rate, exhibit greater secondary phase growth and a higher tendency for Cr_2Nb to cluster.

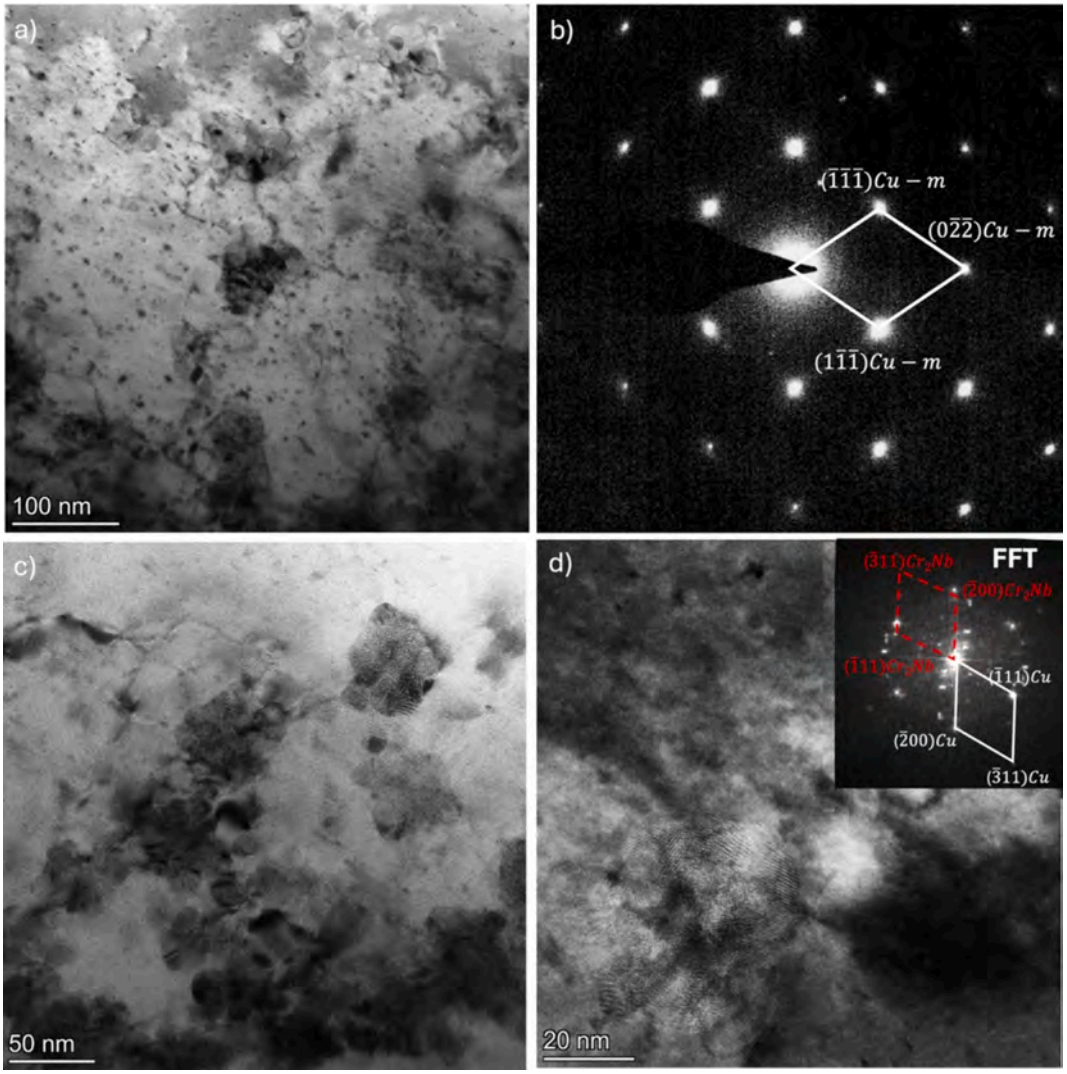

Fig. 5. A) representative bf image showing the detected nanometric precipitation either under the form of single spherical particles either as clusters; b) indexed saedp pattern of (a) reporting the zone axis $[0\ -1\ 1]_{Cu}$; c) representative BF micrograph at higher magnification showing the presence of GPZs, d) HRTEM image displaying a precipitation along with its indexed FFT reporting a FCC cube on cube OR.

IV)[41,42]. The prominent endothermic peak V lies outside the stability range of the previously identified Cu-Cr secondary phases; therefore, a partial contribution can reasonably be attributed to their dissolution [43,44]. With regard to Cr_2Nb, although a limited dissolution of the finer precipitate fraction is reported in literature above 700°C [45], its well-established stability in this system allows to state that wholesale dissolution would occur only at much higher temperatures. Under these premises, considering the remarkable intensity of peak V, a more plausible interpretation is that it represents a composite signal arising from the limited dissolution of fine precipitates in combination with consistent microstructural relaxation processes, such as dislocation annihilation (recovery) and coarsening of existing Cr_2Nb precipitates. Finally, the high temperature exothermic peaks VI and VII may be associated with the precipitation of Nb-rich phases [45], most likely oxides, due to the strong affinity of Nb for oxygen under these processing conditions.

Based on the DSC results, heat treatment temperatures of 400 and 500°C were selected for DAHT in this study. These temperatures are appropriate for controlled aging, as they lie just above the onset of the first precipitation event (Peak I) while remaining below Peaks III and IV, which might be associated with the formation of metastable, incoherent, and potentially detrimental phases.

The impact of post-processing on precipitation behavior was investigated using XRD. Fig. 9 presents the diffraction patterns for all examined conditions. The analysis confirms the presence of the C15-structured Cr_2Nb intermetallic phase even in the as-built condition. Furthermore, refinement of the diffraction patterns using the Rietveld method enabled quantification of lattice parameter variations as a function of heat treatment temperature and duration.

Inset A in Fig. 9 highlights the evolution of the lattice parameter due to solute depletion during precipitation. In the AB condition, diffraction peaks are initially shifted towards lower diffraction angle (corresponding to higher lattice parameters) with respect to pure copper. Upon heat treatment, these peaks progressively shift back towards the reference positions, indicating the formation of Cr_2Nb precipitates and the corresponding reduction in solute content within the Cu matrix. Under these conditions, where Cr and Nb mainly form the stoichiometric Cr_2Nb intermetallic compound, the alloy system can be effectively approximated as a pseudo-binary alloy comprising a Cu-rich matrix and the Cr_2Nb phase. This assumption is further supported by previous studies on similar systems, such as the Cr–Ta–Cu ternary alloy, where it was shown that Cu can substitute Cr in the Cr_2Ta Laves phase without altering its crystal structure or symmetry. Given the structural and chemical similarities between Ta and Nb, as well as the isostructural relationship between Cr_2Nb and Cr_2Ta, it is reasonable to expect that Cu

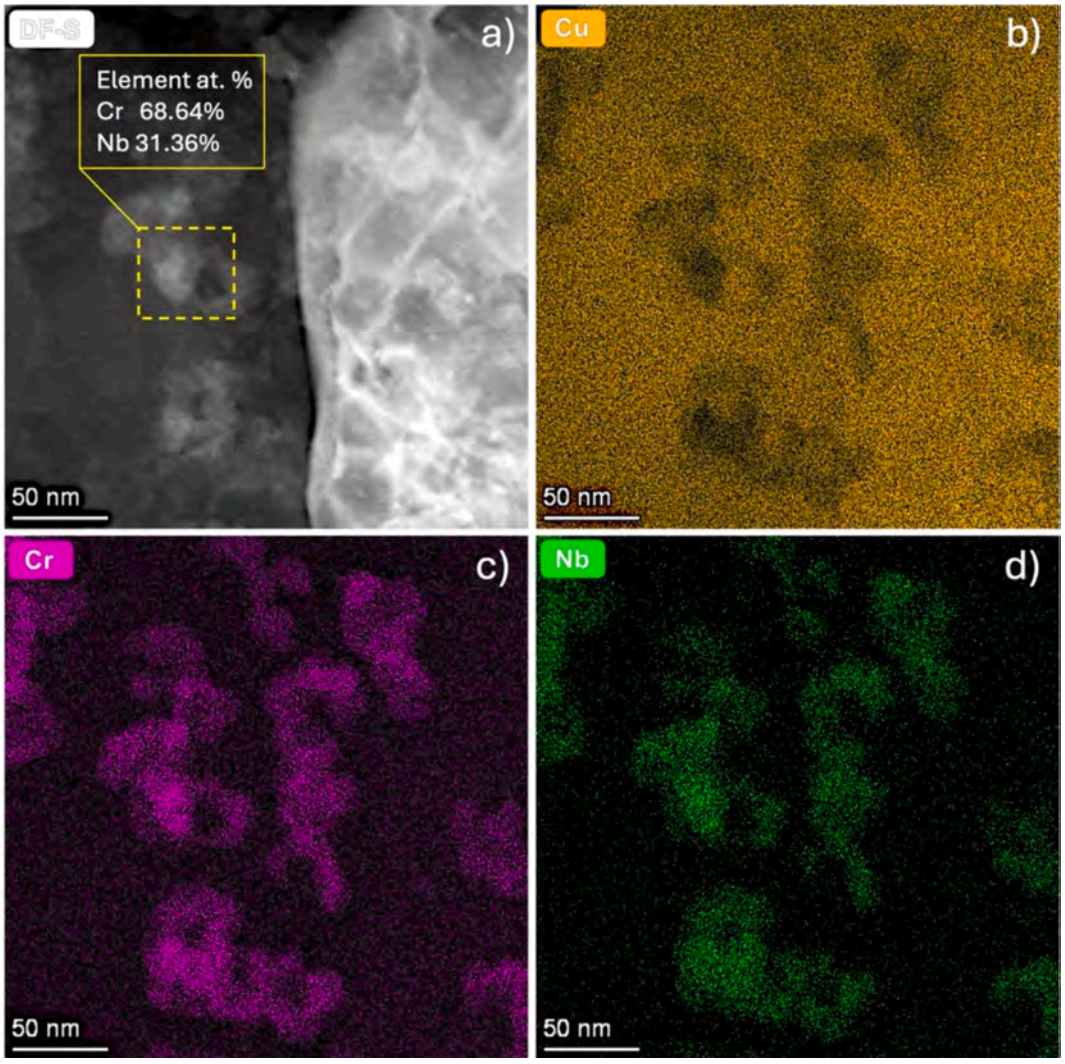

Fig. 6. TEM results of submicron particles: a) Dark-fields (DF) image reporting the composition as at%; b)-c)- d) TEM-EDXS maps of Cu, Cr and Nb elements in a). The composition matches the atomic ratio 2:1 of the Cr_2Nb.

can also be partially accommodated within the Cr_2Nb lattice without destabilizing the phase. As a result, the Cu–Cr_2Nb system behaves in a binary-like manner along this compositional path, justifying the application of Vegard's law to relate lattice parameter changes to the solute content [46].

This interpretation is further validated by the lattice parameter analysis presented in Fig. 10, where the measured values for different aging treatments are plotted against the corresponding mole fraction of alloying elements retained in solid solution. The estimation of the retained solute content within the Cu matrix of the GRCop-42 alloy, as well as the corresponding lattice parameter measurements, were analyzed using Vegard's law as a first-order approximation. According to this model, the lattice parameter varies linearly with the atomic (mole) fraction of solute atoms, and is described by Eq. (5):

$$f = \frac{a - a_{Cu}}{a_{Cr_2Nb} - a_{Cu}} \tag{5}$$

The lattice parameters of pure copper and Cr_2Nb were taken as 3.6150 Å [47] and 6.9805 Å [48], respectively. The maximum lattice parameter observed in the as-built condition, corresponding to the maximum solute content in solid solution, was 3.6282 Å. The alloy composition was assumed as reported in Table 1. Using the atomic weights of Cr (51.996 g/mol), Nb (92.906 g/mol), and Cu (63.546 g/mol), the total number of moles of Cr and Nb per 100 g of alloy was calculated. The fraction f, obtained from the lattice parameter analysis via Vegard's law, was multiplied by the total moles of solute (Cr and Nb) to estimate the amount of solute retained in solid solution. This value was then expressed as a percentage of the total available solute in the alloy, providing a relative measure of solute retention within the Cu matrix across the different heat treatment conditions summarized in Table 3.

The results clearly highlight that temperature has a more significant influence than time in controlling precipitation process. Nearly complete solute depletion is achieved after 3 h at 500°C. In contrast, at 400°C, the lattice parameter reaches an apparent plateau after 5 h, indicating a pronounced slowdown in precipitation kinetics. This behavior implies that Cr_2Nb precipitation at 400°C may follow a logarithmic rate. However, further investigation is required to fully characterize the precipitation kinetics governing the aging behavior of GRCop-42 at different temperatures.

3.4. Direct aging heat treated samples microstructure and coarsening behavior

Regarding the microstructure, a bimodal, and in some cases trimodal, distribution of precipitates was observed across all examined DAHT samples (Figs. 11-12). The largest precipitates, often irregular in shape and referred to as "primary" particles (labeled "A" in Figs. 11a, 11b,

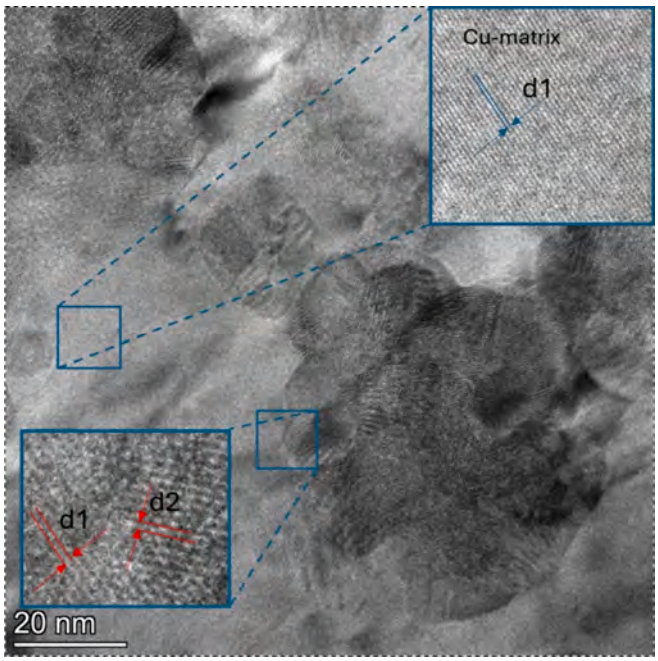

Fig. 7. HRTEM micrograph highlighting the relationship existing along the crystallographic direction (111) for the nanometric Cr-rich phase and the surrounding Cu-matrix. Atomic plane distances d_1 and d_2 were measured from the FFT in the selected areas.

12c), are formed directly from the melt. These are typically located along cell boundaries, characteristic features of the solidification microstructure in L-PBF processed alloys, as previously shown in Fig. 5, and tend to aggregate as the aging conditions become more severe (Fig. 11b, 11c, and 11d), ultimately giving rise to a trimodal distribution. In contrast, "secondary" precipitates (labeled "B" in Figs. 11a, 11b and 12c) nucleate during aging from the supersaturated solid solution.

These precipitates are approximately one order of magnitude smaller than the primary particles and typically exhibit a more spherical morphology. Their presence, however, cannot be fully discarded in the AB condition. This is supported by the finest spherical features in Fig. 11a and by TEM observation reported in Fig. 6a, which suggest that a small fraction of these nanometric precipitates may already form during processing. This can be attributed to local in-situ heat treatment caused by the successive layer deposition, where the accumulated thermal cycles promote partial precipitation in the solid state. As a matter of fact, the high-power input required for processing, as discussed in the previous sections, leads to deep melt pool penetration and the formation of large heat-affected zones adjacent to the scanned tracks (Fig. 3), which could also contribute to the early formation of such secondary particles in the AB state.

Moreover, the secondary precipitates, after aging, can be further divided into two distinct populations: larger clusters, measuring some hundred nanometers (Fig. 12d), and finer particles, generally smaller than 10 nm (Fig. 12c) having a more uniform size distribution, suggesting a correlation of the size and density with the aging parameters. Figs. 13 and 14 present the volume fraction (f_V) and size distribution of the discussed precipitates, derived from high-magnification SEM images. The size distribution is represented as a histogram, normalized to show the percentage of particles within each 10 nm size interval. To quantitatively assess the characteristic precipitate size in a statistically meaningful way, a weighted average diameter d_W was computed. This metric accounts for the relative contribution of each particle to the total measured area, using the formula:

$$d_W = \frac{\sum (d_i \cdot A_i)}{\sum A_i} \tag{6}$$

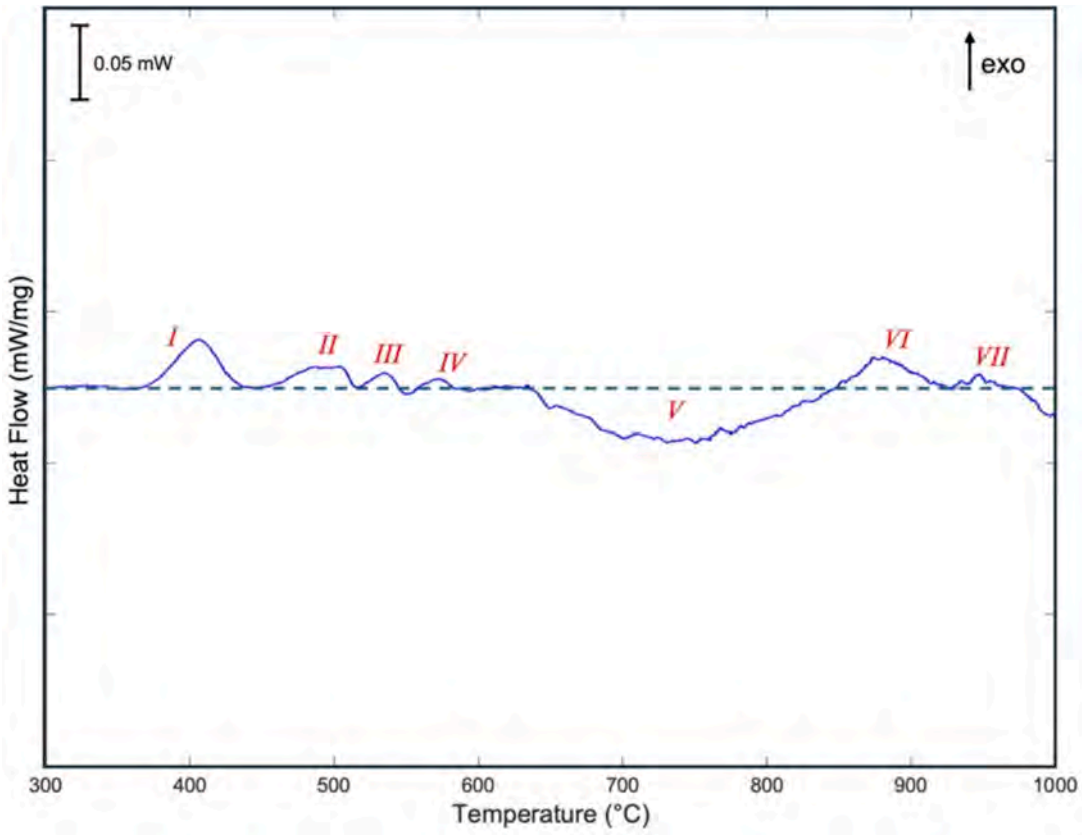

Fig. 8. DSC plot of the L-PBF sample in as-built condition.

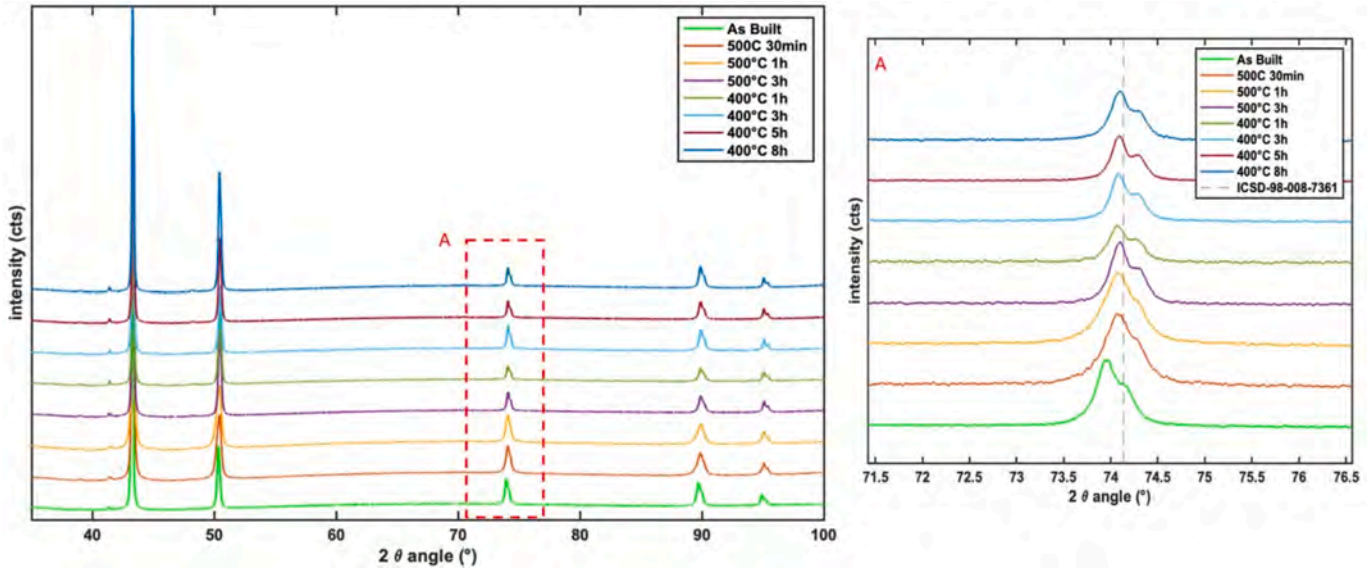

Fig. 9. XRD patterns of CuCrNb alloy samples subjected to various heat treatments, illustrating the influence of thermal processing on the microstructure. The main plot compares diffraction peaks to reveal changes associated with precipitation and microstructural rearrangement. Inset A displays the peak shifting with respect to pure copper (dashed line) due to the variation in lattice parameters, reflecting compositional changes in the matrix as well as strain relaxation associated with the formation of secondary phases.

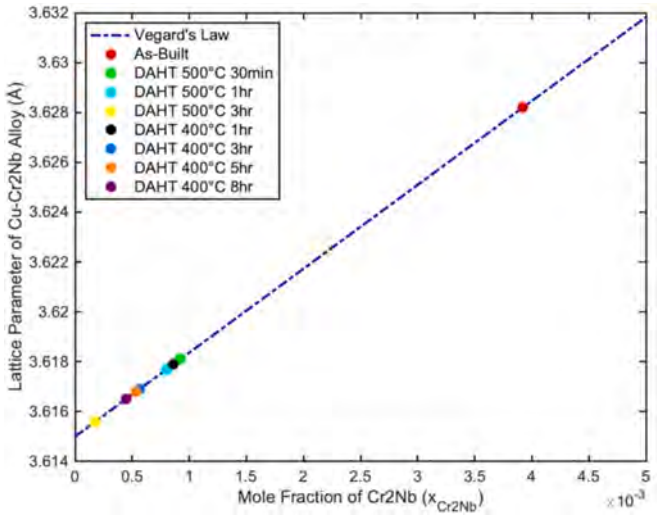

Fig. 10. Lattice parameter of the Cu–Cr_2Nb alloy as a function of the calculated mole fraction of alloying elements retained in solid solution for various Direct Aging Heat Treatments (DAHT). The dashed blue line represents the theoretical prediction based on Vegard's law. Data points correspond to different aging durations at 400 and 500°C. (For interpretation of the references to colour in this figure legend, the reader is referred to the web version of this article.)

where d_i and A_i are the diameter and area of the i-th particle, respectively. This approach emphasizes the contribution of larger precipitates to the overall volume, providing a more representative average particle size. The d_W for each heat treatment condition shows also good agreement with the crystallographic analysis. XRD data (Table 3) suggest that precipitation is promoted at both temperatures, however growth seems to be slower at lower aging temperatures. It should be noted that at 400°C, the formation of a substantial population of spherical secondary precipitates becomes clearly evident only after 5 h of heat treatment (Fig. 12c), with the average particle diameter falling to 25.17 nm, a value comparable to the 26.15 nm observed after just 30 min at 500°C. Although the primary precipitates remain largely unchanged, the emergence of newly nucleated particles alters the statistical distribution,

Table 3
Estimated fraction of alloying elements (Cr and Nb) retained in solid solution in the Cu matrix of GRCop-42, calculated from lattice parameter measurements using linear Vegard's law for each post-build heat-treatment condition.

DAHT Temperature [°C]	DAHT Time [h]	Lattice parameter [Å]	Residual Cr + Nb (as % of total alloy)	Residual Cr + Nb (as % of alloying elements)
As-Built	As-built	3.6282	4.21	65.97
400	1	3.6179	0.92	14.48
400	3	3.6169	0.61	9.49
400	5	3.6168	0.57	8.99
400	8	3.6165	0.48	7.49
500	0.5	3.6181	0.99	15.49
500	1	3.6177	0.86	13.49
500	3	3.6156	0.19	2.99

reducing the overall average size and shift the statistical distribution toward smaller diameters. Furthermore, the FESEM resolution may be insufficient to capture the finest fraction (<10 nm), which are likely present during shorter thermal treatments at 400°C.

This aspect is further highlighted in Fig. 15, which show the cumulative frequency distribution of the precipitates, including the as-built condition, for both the aging conditions. At 400°C, the distributions exhibit minimal changes up to 5 h, whereas at 500°C the data are more dispersed, revealing a clearer distinction between nucleation and growth phases.

Comparing the extended aging treatments, specifically, the 5 h and 8 h conditions at 400°C (Fig. 12c, 12d), indicates that the spatial distribution of precipitates is influenced by grain boundary diffusion. While Ostwald ripening likely contributes to coarsening of the largest precipitates, the histograms show an increasing fraction of fine Cr_2Nb particles with time, suggesting that new nucleation continues to occur even for prolonged aging times. Newly formed intragranular secondary precipitates tend to cluster, and over time, these clusters appear to merge with the growing primary precipitates. This behavior highlights a dynamic and interconnected evolution between the two precipitate populations, indicating that the precipitation process at 400°C involves both coarsening of existing large particles and continuous formation of finer secondary precipitates.

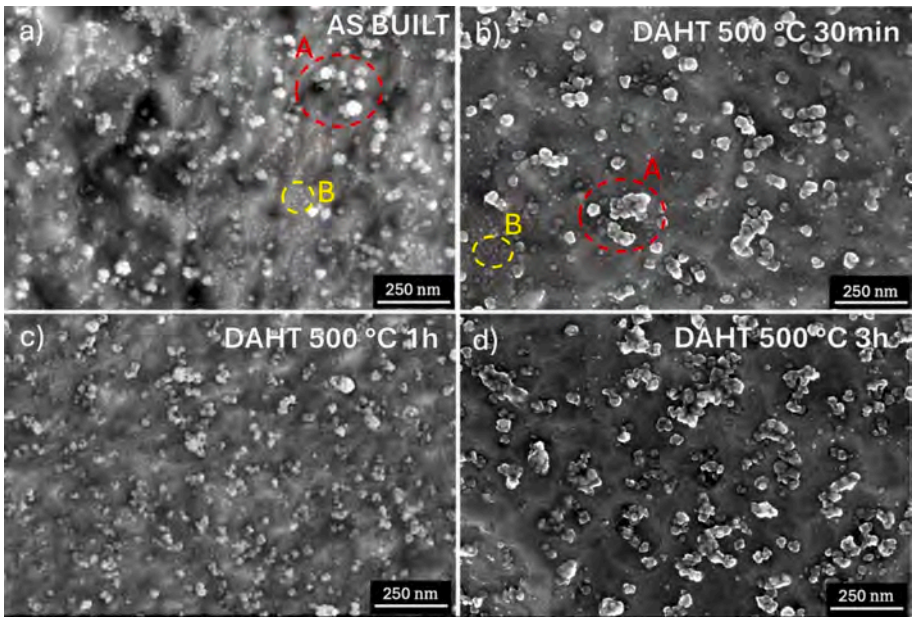

Fig. 11. High magnification micrographs of the different 500°C direct aged conditions, showing the distribution and morphology of the primary particles originated from the melt (A) and the precipitated ones (B): a) As-Built optimized sample; b) DAHT 500°C 30 min; c) DAHT 500°C 1 h; c) DAHT 500°C 3 h.

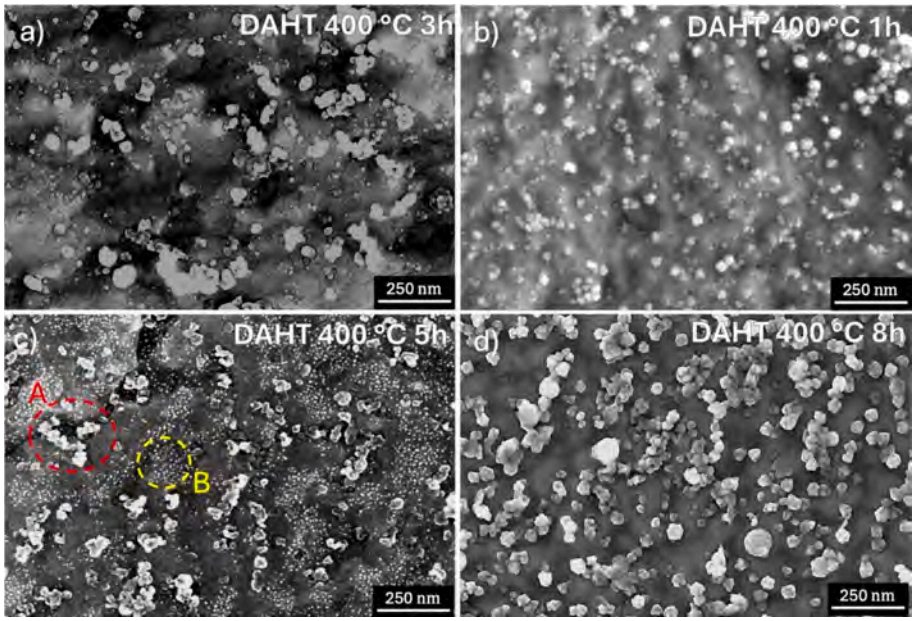

Fig. 12. High magnification micrographs of the different 400°C direct aged conditions, showing the distribution and morphology of the primary particles originated from the melt (A) and the precipitated ones (B): a) DAHT 400°C 1 h condition; b) DAHT 400°C 3 h condition; c) DAHT 400°C 5 h; d) DAHT 400°C 8 h.

These findings provide important insights into the thermal microstructural stability of the alloy. Systems containing precipitates of varying sizes are generally thermodynamically unstable due to the high interfacial energy associated with smaller particles. In such systems, larger precipitates, having lower total interfacial area, tend to grow at the expense of smaller ones, thereby reducing the overall free energy of the system [45]. In the present alloy, analysis of precipitate size distributions across all heat-treated conditions shows that the volume fraction of primary particles remains essentially unchanged. These primary precipitates, which form directly from the liquid phase and reach sizes of approximately 100 nm, exhibit sluggish coarsening and undergo minimal dissolution during subsequent thermal exposure. While they contribute to grain boundary pinning and thus help inhibit grain growth, the fine intragranular secondary precipitates, much smaller than the primary particles, are primarily responsible for hardening, as they provide the high-density obstacles that impede dislocation motion.

To further investigate the implications of precipitate coarsening on microstructural evolution and to better understand the dominant strengthening mechanisms, the KAM mapping was carried out for all heat treated conditions, as reported in Figs. 16 and 17. The analysis of average local misorientation, based on Eq. (1), enabled estimation of the dislocation density and its evolution as a function of aging time. In the AB condition, the alloy exhibits a high dislocation density of approximately 3.87×10^{14} m^{-2}, primarily introduced by the severe thermal gradients inherent to the L-PBF process.

As aging progresses, the dislocation density evolves in accordance

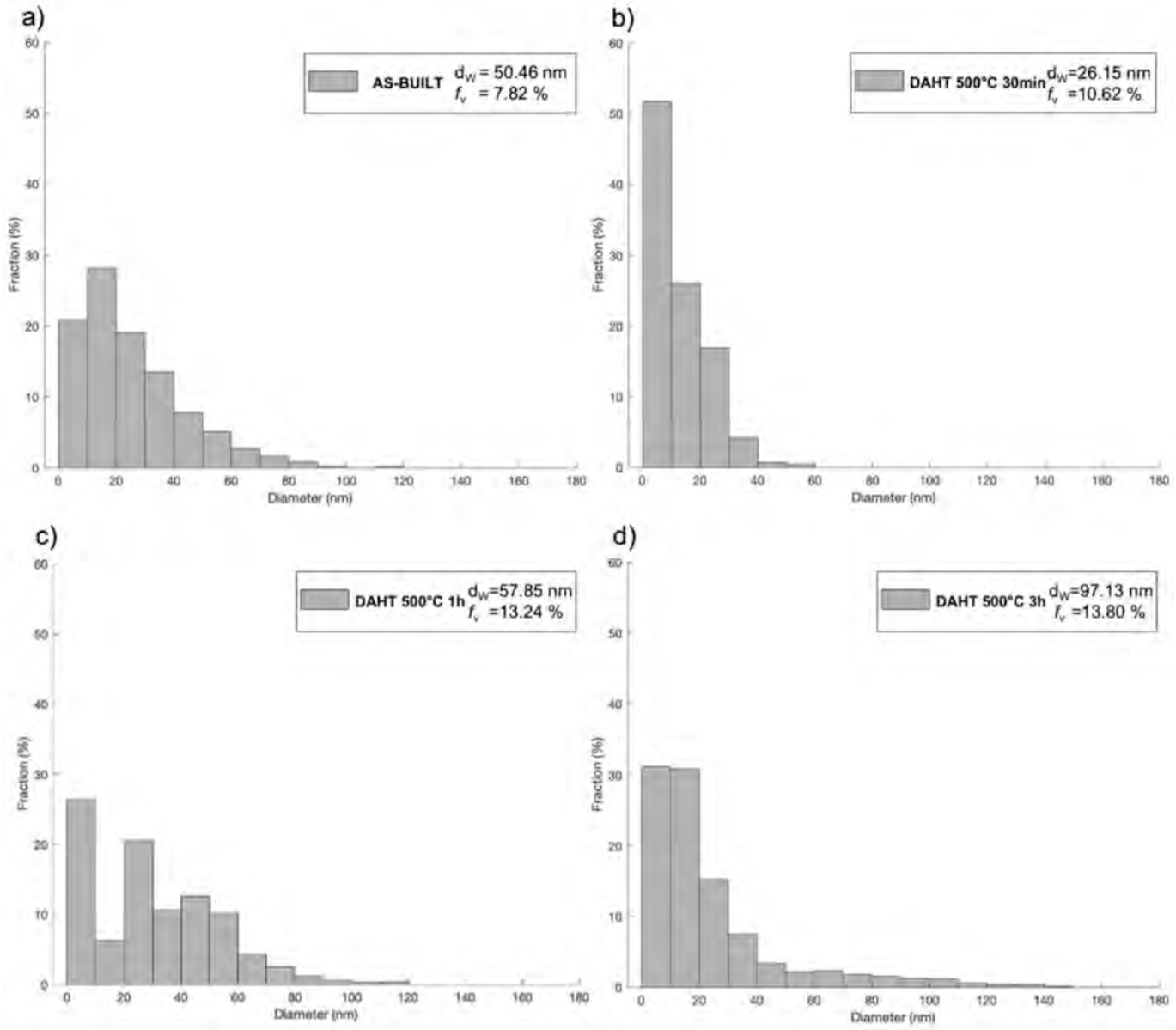

Fig. 13. Statistical evaluation of the size distribution, mean size and volume fraction of the Cr-rich spherical precipitations after the 500°C DAHT conditions: a)As-Built condition; b) DAHT 500°C 30 min; c) DAHT 500°C 1 h; d) DAHT 500°C 3 h.

with the growth behavior of the precipitates. Notably, the density remains relatively stable during the early stages of aging, up to 30 min, maintaining a value of approximately 4.47 × 10^14 m^{-2}. Beyond this point, it decreases sharply by nearly an order of magnitude, reaching approximately 1.41 × 10^14 m^{-2} after 3 h of treatment at 500°C, which corresponds to the onset of over-aging. In contrast, for samples aged at 400°C, where precipitation kinetics are slower, a stable microstructural rearrangement is not observed until after 5 h of aging, at which point the dislocation density stabilizes around 1.14 × 10^14 m^{-2}. This trend strongly supports the mechanism proposed by Takahashi *et al.*[49] and Sato *et al.* [50] on similar precipitation-hardened copper systems, in which dislocation rearrangement occurs simultaneously with precipitate coarsening. Furthermore, at longer aging times, the rate of dislocation density reduction significantly diminishes, suggesting that dislocations within the copper matrix become increasingly stabile. This stabilization indicates that, in addition to precipitation hardening, dislocation structures themselves contribute to the overall strengthening of the alloy under prolonged thermal exposure.

3.5. Direct aging heat treated micro-hardness evolution

Fig. 18 reports the microhardness evolution with aging, providing valuable insights into the strengthening mechanisms in GRCop-42 and the influence of aging time and temperature. According to Gruber *et al.* [21], the hardness of GRCop-42 can range from 103 to 219 HV, depending on the applied heat treatment. The measured hardness of 168 HV in AB condition suggests that the material has undergone a partial in situ aging during processing.

At 400°C, the hardness curve exhibits a progressive increase up to ~ 5 h, followed by a plateau extending to 8 h. This trend is in agreement with both XRD data (Fig. 10), showing a steady reduction in Cr and Nb content in solid solution, and microstructural observations, where spherical fine precipitates remain visible even after 8 h of treatment. The stability of the hardness values during prolonged aging is therefore consistent with a state where precipitation is still active but not accompanied by a significant over-aging.

At 500°C, an abrupt hardness increase is observed within the first

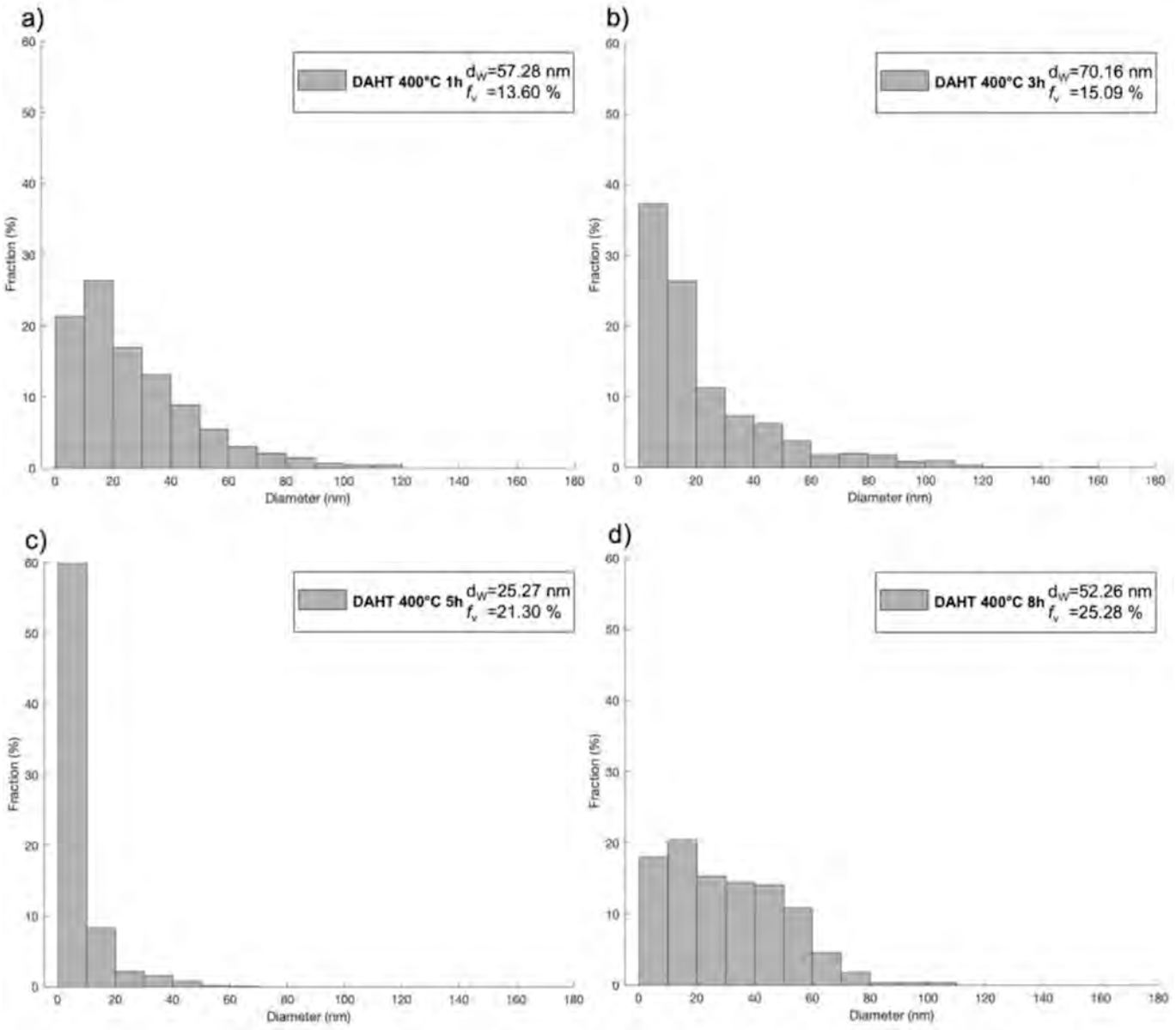

Fig. 14. Statistical evaluation of the size distribution, mean size and volume fraction of the Cr-rich spherical precipitations after the 400°C DAHT conditions: b) DAHT 400°C 1 h; c)DAHT 400°C 3 h; d)DAHT 400°C 5 h; e)DAHT 400°C 8 h.

hour, reaching a maximum of ~ 260 HV, followed by a gradual decrease with longer times. This behavior is in line with XRD results indicating that nearly all Cr and Nb have precipitated from the supersaturated solid solution during the early stage of aging. Microstructural analysis confirms this condition, showing coarsening of the finest precipitates, which reduces the effectiveness of precipitation strengthening. While precipitates smaller than ~ 10 nm are not detected in SEM microscopy observations, their presence cannot be excluded and should be confirmed by TEM analysis.

To better understand this relatively high hardness value in the AB condition, it is essential to refer to the literature and examine the typical strengthening mechanisms operating in this class of alloys. In general, metallic materials are strengthened through four main mechanisms:

(1) Grain boundary strengthening (Hall-Petch effect): finer grains impede dislocation movement due to increased grain boundary area.
(2) Solid solution strengthening: solute atoms dissolved in the matrix generate lattice distortions that hinder dislocation motion.
(3) Dislocation strengthening: the interaction and accumulation of dislocations increase resistance to plastic deformation.
(4) Precipitation strengthening: the presence of nanoscale second-phase particles impedes dislocation motion, typically via the Orowan mechanism.

In precipitation-hardenable cooper-based alloys, such as GRCop-42, precipitation strengthening is the dominant mechanism, particularly due to the formation of nanoscales Cr_2Nb particles. The strengthening effect from precipitates can be quantitatively described by the Orowan mechanism, which relates the increase in yield strength, $\Delta\sigma_{PS}$, to precipitate characteristics via the following relation [51]:

$$\Delta\sigma_{PS} = \frac{0,8MGb}{2\pi\sqrt{1-\nu}} \frac{\ln\left(\frac{2r}{b}\right)}{\lambda - 2r} \tag{7}$$

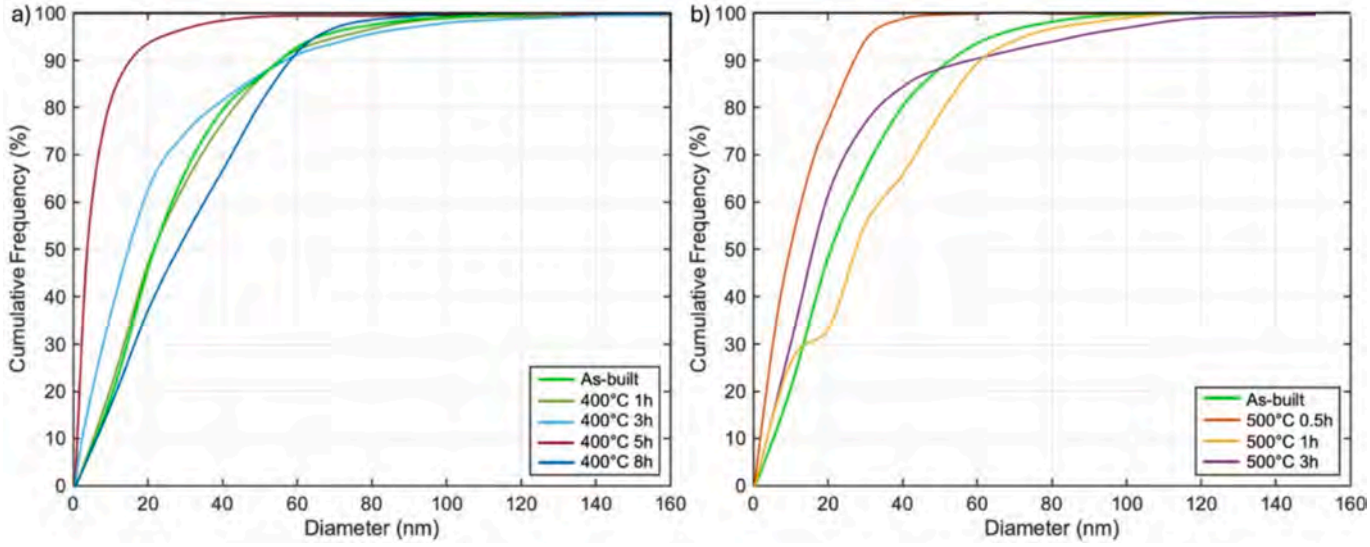

Fig. 15. Cumulative frequency distributions of secondary precipitates in the alloy, including the as-built condition, for aging at 400°C (a) and 500°C (b).

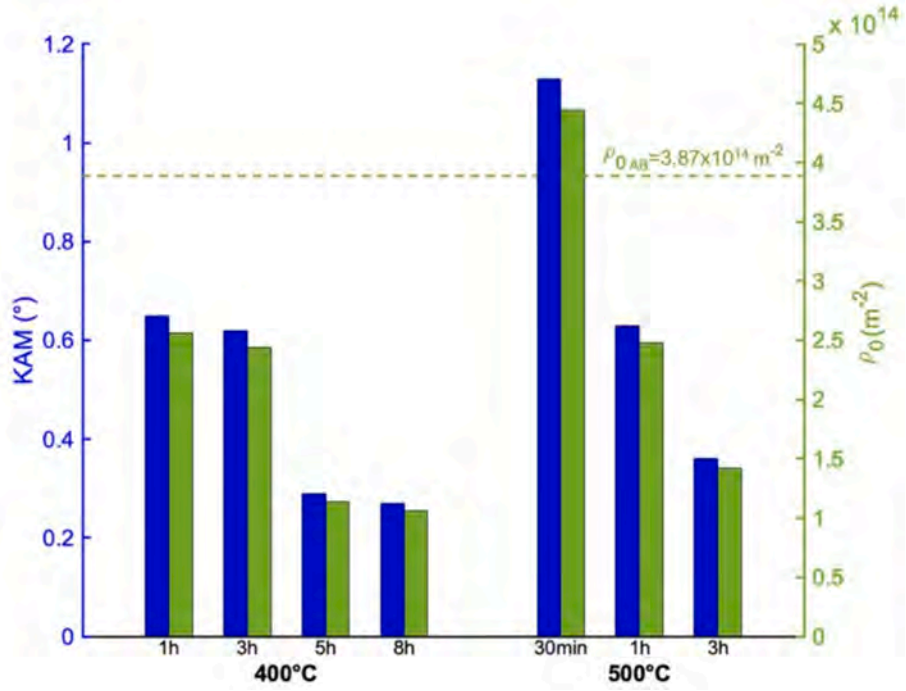

Fig. 16. Bar chart comparing the local misorientation and dislocation density and variation over temperature and time.

where M is the Taylor factor, G is the shear modulus of the copper matrix, b is the matrix Burgers vector, r is the average radius of the precipitates, ν is the Poisson's ratio, and λ is the average inter-precipitate spacing on the slip plane. The value λ can be estimated as a function of the volumetric fraction of precipitates, f_V, assuming a uniform spherical distribution of precipitates, using the following relationship [16,51]:

$$\lambda = r\left(\sqrt{\frac{2\pi}{3f_V}} - 1,63\right) \tag{8}$$

From Eq (7) and Eq. (8), it is evident that precipitate radius and volume fraction are the most influential parameters governing the Orowan strengthening effect. Based on the previously discussed microstructural transformations, all major strengthening mechanisms are thus active in the AB condition. The L-PBF process is particularly effective in retaining ~ 65% of alloying elements in solid solution (Fig. 10), while the formation of a dense dislocation network induced by steep thermal gradients further enhances strengthening.

Although Orowan strengthening is already active in the AB condition, as indicated by a measured precipitate volume fraction of 7.8% (Fig. 13a), its contribution becomes significantly more pronounced after aging. At 500°C, coarsening of precipitates after peak hardness leads to a calculated ~ 27% reduction in the Orowan strengthening contribution, which is consistent with the experimentally observed hardness decrease of 15.2 ± 7% especially considering that the dislocation density remains largely unchanged from the peak-aging condition. In contrast, aging at 400°C produces a stable hardness response, reflecting the balance between continued precipitation and limited coarsening, with no evident signs of over-aging up to 8 h. Therefore, precipitation strengthening remains the dominant mechanism throughout the aging period.

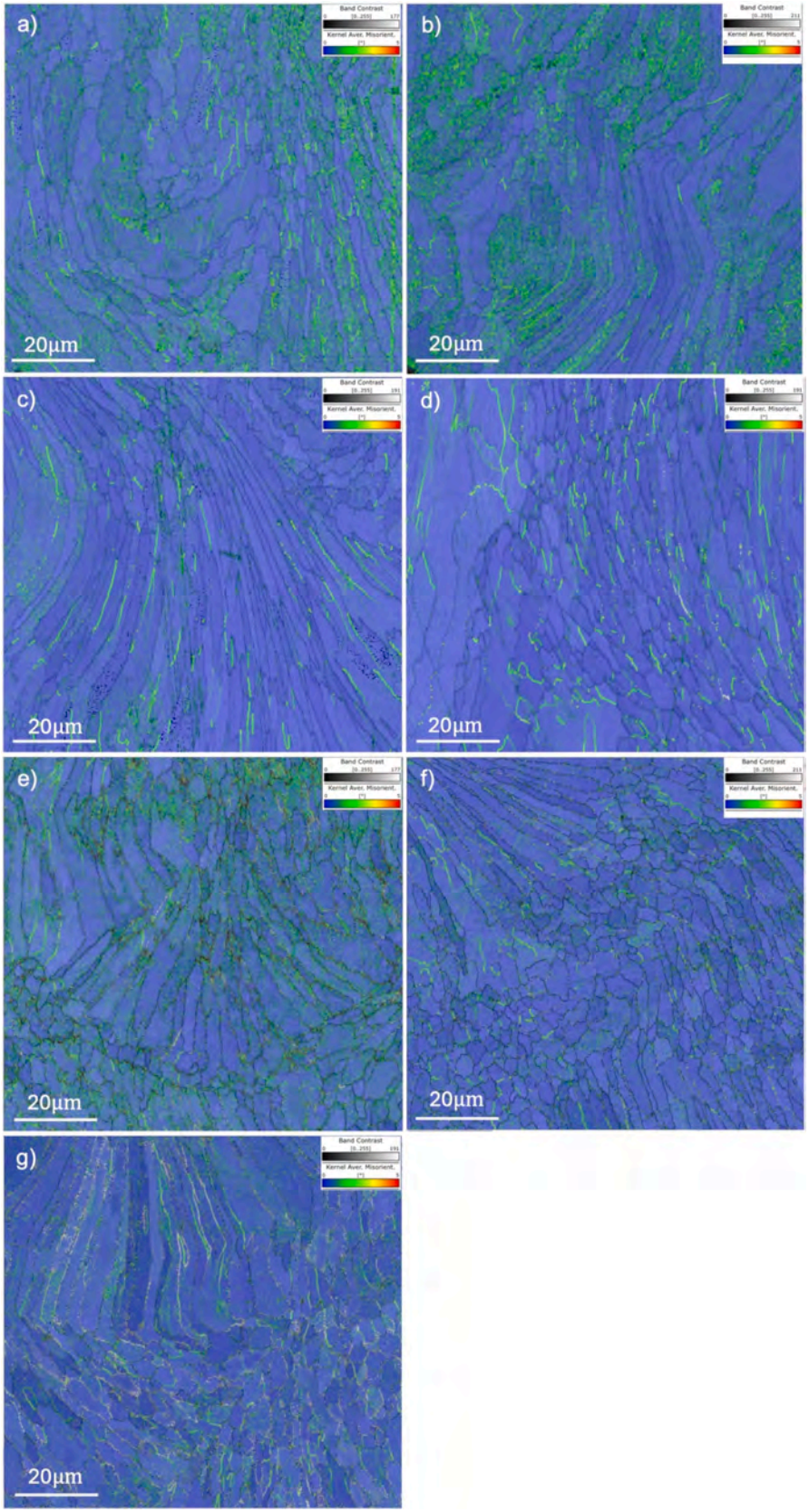

Fig. 17. Kernel Average Misorientation mapping for all the DAHT investigated:, a) 400°C 1 h; b) 400°C 3 h; c) 400°C 5 h; d) 400°C 8 h; r) 500°C 30 min; f) 500°C 1 h; g) 500°C 3 h.

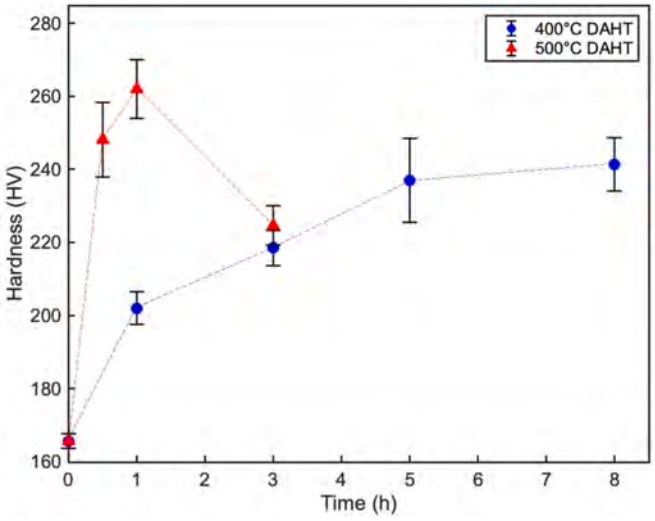

Fig. 18. Average microhardness comparison for the different heat-treated conditions showing the strengthening effect of temperature and time.

4. Conclusions

In this study, the microstructural evolution and precipitation behavior of L-PBF processed GRCop-42 were thoroughly investigated in as-built and under various DAHT post-process conditions. The L-PBF process enabled the production of high-density components (99.7%) with tailored microstructural features. The main conclusions are summarized as follows:

- Due to the extremely rapid cooling rates inherent to the L-PBF process, a homogeneous dispersion of fine precipitates was achieved throughout the matrix. However, non-uniform thermal gradients within the molten pool led to a bimodal distribution of these precipitates in the as-built condition. In particular, the secondary phase formed during solidification was identified as FCC C15 Cr_2Nb, exhibiting a cube-on-cube orientation relationships with the cooper matrix $(1\bar{1}\bar{1})Cu \| (1\bar{1}\bar{1})Cr_2Nb$ and $(0\bar{2}\bar{2})Cu \| (0\bar{2}\bar{2})Cr_2Nb$.
- The significant amount of retained solute in the as-built condition enables direct aging within the 400–500°C range without prior solutioning. Precipitation kinetics were found to be strongly temperature dependent. At 500°C, diffusion is very rapid, resulting in complete precipitation within 3 h; however, this also triggers uncontrolled coarsening and rapid over-aging. In contrast, at 400°C, nucleation and growth proceed simultaneously at a slower rate, preventing coarsening even during prolonged aging time.
- The primary strengthening mechanisms in this system are dislocation strengthening and precipitation hardening via Orowan mechanism. The remarkably high hardness observed in the as-built condition is attributed to a dense network of dislocations generated by severe thermal gradients during manufacturing as well as the minor presence of an ultrafine Cr_2Nb precipitate distribution. Upon aging, the dislocation structure reorganizes, contributing to a more stable strengthening effect. Additional strengthening arises from the formation of ultrafine Cr_2Nb precipitates, some of which are below the resolution limit of SEM.

Overall, these findings demonstrate that L-PBF is a highly effective route for manufacturing GRCop-42 components designed for high thermal flux environments. The unique thermal history and localized solidification conditions, intrinsic to L-PBF, yield a characteristic microstructure distinct from conventionally processed counterparts, offering new opportunities for performance optimization. However, further mechanical testing is necessary to fully assess the long-term thermal and mechanical stability of the alloy, especially concerning precipitate coarsening and its influence on properties. Further work is also necessary to understand the kinetics of the strengthening mechanisms and their interactions under service-relevant conditions.

CRediT authorship contribution statement

Stefano Felicioni: Writing – original draft, Investigation, Conceptualization. **Adrian Barbosa Cantu:** Validation, Investigation, Formal analysis. **Elisa Padovano:** Writing – review & editing, Supervision, Methodology. **Angela Veiga:** Writing – review & editing, Supervision, Methodology, Data curation, Conceptualization. **Miren Aristizabal:** Supervision, Methodology, Investigation. **Nerea Ordás:** Writing – review & editing, Validation, Supervision, Project administration, Methodology, Funding acquisition. **Federica Bondioli:** Writing – review & editing, Supervision, Methodology, Data curation, Conceptualization.

Declaration of competing interest

The authors declare that they have no known competing financial interests or personal relationships that could have appeared to influence the work reported in this paper.

Acknowledgments

This research did not receive any specific grant from funding agencies in the public, commercial, or not-for-profit sectors.

Data availability

Data will be made available on request.

References

[1] R.J. Schwighamer, «MATERIALS AND PROCESSES FOR SHUTTLE ENGINE, EXTERNAL TANK, AND SOLID ROCKET BOOSTER», in *a New Era in Space Transportation*, Elsevier (1977) 71–88, https://doi.org/10.1016/B978-0-08-021710-9.50013-6.

[2] D. L. Ellis e M. M. Gary, «Precipitation Strengthened High Strength, High Conductivity Cu-Cr-Nb Alloys Produced by Chill Block Melt Spinning», Case Western University, Cleveland, OH, US, Dissertation NASA-CR-185144, set. 1989. [Online]. Disponibile su: https://ntrs.nasa.gov/citations/19900002537.

[3] W. He, E. Wang, L. Hu, Y. Yu, e H. Sun, «Effect of extrusion on microstructure and properties of a submicron crystalline Cu–5wt.%Cr alloy», *J. Mater. Process. Technol.*, vol. 208, fasc. 1–3, pp. 205–210, nov. 2008, doi: 10.1016/j.jmatprotec.2007.12.107.

[4] M. A. Morris e D. G. Morris, «MICROSTRCTURE AND MECHANICAL PROPERTIES OF RAPIDLY SOLIDIFIED Cu Cr ALLOYS», *Acta Metall. Sin.*, vol. Vol. 35, fasc. 10, pp. 2511–2522, 1987, doi: 000I-6160/87.

[5] D. L. Ellis, «GRCop-84: A High-Temperature Copper Alloy for High-Heat-Flux Applications», NASA Glenn Research centre, Glenn Research Center, Technical Memorandum (TM) NASA/TM-2005-213566, 2005. [Online]. Disponibile su: https://ntrs.nasa.gov/citations/20050123582.

[6] P. R. Gradl, D. C. S. Protz, D. D. L. Ellis, e S. E. Greene, «Progress in Additively Manufactured Copper-Alloy GRCop-84, GRCop-42, and Bimetallic Combustion Chambers for Liquid Rocket Engines», in *th International Astronautical Congress*, Washington, DC: International Astronautical Federation (IAF-HQ), ott. 2019. [Online]. Disponibile su: https://ntrs.nasa.gov/citations/20190033311.

[7] H. C. De Groh, D. L. Ellis, e W. S. Loewenthal, «Comparison of GRCop-84 to Other Cu Alloys with High Thermal Conductivities», *J. Mater. Eng. Perform.*, vol. 17, fasc. 4, pp. 594–606, ago. 2008, doi: 10.1007/s11665-007-9175-3.

[8] A. D. Iams, T. J. Lienert, D. A. Otazu, e M. Ramoni, «Effects of deposition sequence on microstructural evolution in additively manufactured Cu-Cr-Nb alloy / superalloy bimetallic structures», *Addit. Manuf. Lett.*, vol. 6, p. 100151, lug. 2023, doi: 10.1016/j.addlet.2023.100151.

[9] Z. Q. Yang *et al.*, «Role of crystal defects on brittleness of C15 Cr2Nb Laves phase», *Acta Mater.*, vol. 60, fasc. 6–7, pp. 2637–2646, apr. 2012, doi: 10.1016/j.actamat.2012.01.030.

[10] G. Demeneghi, P. Gradl, J. R. Mayeur, e K. Hazeli, «Size effect characteristics and influences on fatigue behavior of laser powder bed fusion of thin wall GRCop-42 copper alloy», *Heliyon*, vol. 10, fasc. 7, p. e28679, apr. 2024, doi: 10.1016/j.heliyon.2024.e28679.

[11] J. C. Williams, A. W. Thompson, J. I. Tien, e J. I. Elliot, «Strengthening of metals and alloys», *Metall. Treatises*, pp. 487–504, 1981.

[12] D. J. Chakrabarti e D. E. Laughlin, «The Cr-Cu (Chromium-Copper) system», vol. Vol. 5, fasc. Bulletin of Alloy Phase Diagrams, pp. 59–67, 1984, doi: https://doi.org/10.1007/bf02868727.
[13] H. Okamoto, «Section III: Supplemental Literature Review», *J. Phase Equilibria*, vol. 19, fasc. 5, pp. 486–486, ott. 1998, doi: 10.1007/BF02700865.
[14] R. Anderson, «High Temperature Coarsening of Cr2Nb Precipitates in Cu-8 Cr-4 Nb Alloy», California University, Davis, CA, USA, Dissertation, giu. 1996. [Online]. Disponibile su: https://ntrs.nasa.gov/citations/19960028089.
[15] K. R. Anderson e J. R. Groza, «Microstructural size effects in high-strength high-conductivity Cu-Cr-Nb alloys», *Metall. Mater. Trans. A*, vol. 32, fasc. 5, pp. 1211–1224, mag. 2001, doi: 10.1007/s11661-001-0130-x.
[16] E. Orowan, FRACTURE AND STRENGTH OF SOLIDS, Prog. Phys. vol. 12, fasc. 1 (1949) 185–232, https://doi.org/10.1088/0034-4885/12/1/309.
[17] P. R. Gradl e C. S. Protz, «Technology advancements for channel wall nozzle manufacturing in liquid rocket engines», *Acta Astronaut.*, vol. 174, pp. 148–158, set. 2020, doi: 10.1016/j.actaastro.2020.04.067.
[18] P. R. Gradl, C. S. Protz, K. Cooper, D. Ellis, L. J. Evans, e C. Garcia, «GRCop-42 Development and Hot-fire Testing Using Additive Manufacturing Powder Bed Fusion for Channel-cooled Combustion Chambers», in *AIAA Propulsion and Energy 2019 Forum*, Indianapolis, IN: American Institute of Aeronautics and Astronautics, ago. 2019. doi: 10.2514/6.2019-4228.
[19] P. Gradl *et al.*, «Robust Metal Additive Manufacturing Process Selection and Development for Aerospace Components», *J. Mater. Eng. Perform.*, vol. 31, fasc. 8, pp. 6013–6044, ago. 2022, doi: 10.1007/s11665-022-06850-0.
[20] B. Zheng, Y. Zhou, J. E. Smugeresky, J. M. Schoenung, e E. J. Lavernia, «Thermal Behavior and Microstructure Evolution during Laser Deposition with Laser-Engineered Net Shaping: Part II. Experimental Investigation and Discussion», *Metall. Mater. Trans. A*, vol. 39, fasc. 9, pp. 2237–2245, set. 2008, doi: 10.1007/s11661-008-9566-6.
[21] S. Gruber *et al.*, «Process development for laser powder bed fusion of GRCop-42 using a 515 nm laser source», *J. Laser Appl.*, vol. 35, fasc. 4, p. 042078, nov. 2023, doi: 10.2351/7.0001139.
[22] G. Demeneghi, B. Barnes, P. Gradl, J. R. Mayeur, e K. Hazeli, «Size effects on microstructure and mechanical properties of additively manufactured copper–chromium–niobium alloy», *Mater. Sci. Eng. A*, vol. 820, p. 141511, lug. 2021, doi: 10.1016/j.msea.2021.141511.
[23] B09 Committee, *Test Method for Density of Powder Metallurgy (PM) Materials Containing Less Than Two Percent Porosity*, 13 settembre 2022. doi: 10.1520/B0311-22.
[24] A. P. Zhilyaev, I. Shakhova, A. Morozova, A. Belyakov, e R. Kaibyshev, «Grain refinement kinetics and strengthening mechanisms in Cu–0.3Cr–0.5Zr alloy subjected to intense plastic deformation», *Mater. Sci. Eng. A*, vol. 654, pp. 131–142, gen. 2016, doi: 10.1016/j.msea.2015.12.038.
[25] U. Holzwarth e H. Stamm, «The precipitation behaviour of ITER-grade Cu–Cr–Zr alloy after simulating the thermal cycle of hot isostatic pressing», *J. Nucl. Mater.*, vol. 279, fasc. 1, pp. 31–45, mar. 2000, doi: 10.1016/S0022-3115(99)00285-8.
[26] E04 Committee, «Test Method for Microindentation Hardness of Materials», ASTM International. doi: 10.1520/E0384-22.
[27] X. Tang, X. Chen, F. Sun, P. Liu, H. Zhou, e S. Fu, «The current state of CuCrZr and CuCrNb alloys manufactured by additive manufacturing: A review», *Mater. Des.*, vol. 224, p. 111419, dic. 2022, doi: 10.1016/j.matdes.2022.111419.
[28] F. Calignano, A. Bove, e M. Pavese, «Processing of pure copper by powder bed fusion with infrared laser», *Results Eng.*, vol. 25, p. 104497, mar. 2025, doi: 10.1016/j.rineng.2025.104497.
[29] M. Bayat *et al.*, «Keyhole-induced porosities in Laser-based Powder Bed Fusion (L-PBF) of Ti6Al4V: High-fidelity modelling and experimental validation», *Addit. Manuf.*, vol. 30, p. 100835, dic. 2019, doi: 10.1016/j.addma.2019.100835.
[30] W. E. King *et al.*, «Observation of keyhole-mode laser melting in laser powder-bed fusion additive manufacturing», *J. Mater. Process. Technol.*, vol. 214, fasc. 12, pp. 2915–2925, dic. 2014, doi: 10.1016/j.jmatprotec.2014.06.005.
[31] B. J. Simonds *et al.*, «The causal relationship between melt pool geometry and energy absorption measured in real time during laser-based manufacturing», *Appl. Mater. Today*, vol. 23, p. 101049, giu. 2021, doi: 10.1016/j.apmt.2021.101049.
[32] Y. A. Mayi, M. Dal, P. Peyre, M. Bellet, e R. Fabbro, «Physical mechanisms of conduction-to-keyhole transition in laser welding and additive manufacturing processes», *Opt. Laser Technol.*, vol. 158, p. 108811, feb. 2023, doi: 10.1016/j.optlastec.2022.108811.
[33] L.-J. Zhang, G.-F. Zhang, J. Ning, X.-J. Zhang, e J.-X. Zhang, «Microstructure and properties of the laser butt welded 1.5-mm thick T2 copper joint achieved at high welding speed», *Mater. Des.*, vol. 88, pp. 720–736, dic. 2015, doi: 10.1016/j.matdes.2015.09.072.
[34] S. Geng, P. Jiang, X. Shao, L. Guo, e X. Gao, «Heat transfer and fluid flow and their effects on the solidification microstructure in full-penetration laser welding of aluminum sheet», *J. Mater. Sci. Technol.*, vol. 46, pp. 50–63, giu. 2020, doi: 10.1016/j.jmst.2019.10.027.
[35] C. Selcuk, «Laser metal deposition for powder metallurgy parts», *Powder Metall.*, vol. 54, fasc. 2, 2013, doi: doi.org/10.1179/174329011X12977874589924.
[36] A. Saboori *et al.*, «An investigation on the effect of powder recycling on the microstructure and mechanical properties of AISI 316L produced by Directed Energy Deposition», *Mater. Sci. Eng. A*, vol. 766, p. 138360, ott. 2019, doi: 10.1016/j.msea.2019.138360.
[37] Y. Yang *et al.*, «Cr-based second phases in a high conductivity Cu-Cr-Nb alloy with high high-temperature strength», *Mater. Des.*, vol. 219, p. 110784, lug. 2022, doi: 10.1016/j.matdes.2022.110784.
[38] X. Guo *et al.*, «Microstructure and properties of Cu-Cr-Nb alloy with high strength, high electrical conductivity and good softening resistance performance at elevated temperature», *Mater. Sci. Eng. A*, vol. 749, pp. 281–290, mar. 2019, doi: 10.1016/j.msea.2019.02.036.
[39] L. Peng *et al.*, «The phase transformation and strengthening of a Cu-0.71 wt% Cr alloy», *J. Alloys Compd.*, vol. 708, pp. 1096–1102, giu. 2017, doi: 10.1016/j.jallcom.2017.03.069.
[40] L. G. Vettraino *et al.*, «Influence of processing on the microstructure of Cu–8Cr–4Nb», *J. Mater. Sci.*, vol. 43, fasc. 19, pp. 6546–6555, ott. 2008, doi: 10.1007/s10853-008-2802-z.
[41] X. J. Liu, Z. P. Jiang, C. P. Wang, e K. Ishida, «Experimental determination and thermodynamic calculation of the phase equilibria in the Cu–Cr–Nb and Cu–Cr–Co systems», *J. Alloys Compd.*, vol. 478, fasc. 1–2, pp. 287–296, giu. 2009, doi: 10.1016/j.jallcom.2008.11.162.
[42] J. G. Costa Neto, S. G. Fries, H. L. Lukas, S. Gama, e G. Effenberg, «Thermodynamic optimisation of the Nb-Cr system», *Calphad*, vol. 17, fasc. 3, pp. 219–228, lug. 1993, doi: doi.org/10.1016/0364-5916(93)90001-R.
[43] J. Guo, J. Rosalie, R. Pippan, e Z. Zhang, «On the phase evolution and dissolution process in Cu-Cr alloys deformed by high pressure torsion», *Scr. Mater.*, vol. 133, pp. 41–44, mag. 2017, doi: 10.1016/j.scriptamat.2017.02.009.
[44] L. Shan, L. Yang, e Y. Wang, «Improving the high temperature mechanical performance of Cu–Cr alloy induced by residual nano-sized Cr precipitates», *Mater. Sci. Eng. A*, vol. 845, p. 143250, giu. 2022, doi: 10.1016/j.msea.2022.143250.
[45] K. R. Anderson, J. R. Groza, R. L. Dreshfield, e D. Ellis, «High-Performance dispersion-strengthened Cu-8 Cr-4 Nb alloy», *Metall. Mater. Trans. A*, vol. 26, fasc. 9, pp. 2197–2206, set. 1995, doi: 10.1007/BF02671235.
[46] K. KUOt, «TERNARY LAVES AND SIGMA-PHASES OF TRANSITION METALS», *ACTA Metall.*, vol. 1, fasc. 6, p. 770 724, nov. 1953, doi: https://doi.org/10.1016/0001-6160(53)90031-5.
[47] M. E. Straumanis, «Lattice Parameters, Densities, Expansion Coefficients and Perfection of Structure of Cu and of Cu-In α phase», *Acta Crystallogr. Sect. A*, vol. Volume 25, fasc. Issue 6, pp. 676–682, nov. 1969, doi: https://doi.org/10.1107/S0567739469001549.
[48] R. P. Elliott e W. Rostoker, «The occurence of Laves-type phases among transition elements», *Occur. Laves-Type Phases Transit. Elem.*, vol. 50, pp. 617–633, 1958.
[49] Y. Takahashi, T. Sanada, S. Sato, T. Okajima, K. Shinoda, e S. Suzuki, «SAXS and XAFS Characterization of Precipitates in a High-Performance Cu–Ni–Si Alloy», *Mater. Trans.*, vol. 48, fasc. 2, pp. 101–104, 2007, doi: 10.2320/matertrans.48.101.
[50] S. Sato, Y. Takahashi, K. Wagatsuma, e S. Suzuki, «Characterization of aging behavior of precipitates and dislocations in copper-based alloys», *Powder Diffr.*, vol. 25, fasc. 2, pp. 104–107, giu. 2010, doi: 10.1154/1.3416942.
[51] J. Chen, J. Wang, X. Xiao, H. Wang, H. Chen, e B. Yang, «Contribution of Zr to strength and grain refinement in Cu Cr Zr alloy», *Mater. Sci. Eng. A*, vol. 756, pp. 464–473, mag. 2019, doi: 10.1016/j.msea.2019.04.053.